

Structure and Dynamics of the Young Massive Star Cluster Westerlund 1

LINGFENG WEI (魏凌枫) ¹, JESSICA R. LU ², PETER C. BOYLE,² MATTHEW W. HOSEK JR. ³,
QUINN M. KONOPACKY ⁴, RICHARD G. SPENCER ⁵, DONGWON KIM ⁶, NICHOLAS Z. RUI ⁷, MAX SERVICE,⁸
D. B. HUANG,⁹ AND JAY ANDERSON¹⁰

¹*Department of Physics, University of California, San Diego, La Jolla, CA 92093, USA*

²*Department of Astronomy, University of California, Berkeley, Berkeley, CA 94720, USA*

³*Department of Physics and Astronomy, University of California, Los Angeles, Los Angeles, CA 90095, USA*

⁴*Department of Astronomy and Astrophysics, University of California, San Diego, La Jolla, CA 92093, USA*

⁵*National Institute on Aging, National Institutes of Health, Baltimore, MD 21224, USA*

⁶*Mathpresso, Inc., 17F, WeWork Seolleung Station III, 428, Seolleung-ro, Gangnam-gu, Seoul 06192, Republic of Korea*

⁷*TAPIR, California Institute of Technology, Pasadena, CA 91125, USA*

⁸*W. M. Keck Observatory, 65-1120 Mamalahoa Hwy, Kamuela, HI 96743, USA*

⁹*Verkada Inc., 406 E. 3rd Avenue, San Mateo, CA 94401, USA*

¹⁰*Space Telescope Science Institute, Baltimore, MD 21218, USA*

ABSTRACT

We present a structural analysis of the young massive star cluster Westerlund 1 (Wd 1). With multi-epoch Hubble Space Telescope (HST) observations, we measure the proper motions of 10,346 stars and determine their kinematic memberships by fitting a Gaussian mixture model to their proper motions. After correcting for extinction and completeness, we model the stellar density distribution and confirm the presence of an elongation with an eccentricity of 0.71. The eccentricity decreases slightly with increasing mass. We fit the radial profile with the Elson, Fall, and Freeman model, observing a decrease in the core radius with increasing mass, indicative of weak but detectable mass segregation. This finding is further supported by a measured mass segregation ratio of $\Lambda_{\text{MSR}} = 1.11 \pm 0.11$, only above 1 by 1σ , and slightly shorter minimum spanning tree length for higher mass bins. The cluster has a 1D velocity dispersion of $3.42 \pm 0.10 \text{ km s}^{-1}$, suggesting it is subvirial. The subvirial state implies either exceptionally high star formation efficiency or inefficient stellar feedback caused by local gas expulsion before stars reach the cluster. The crossing time is 0.30 Myr and the relaxation time is 0.26 Gyr. Given the age of Wd 1 of 10.7 Myr, we expect evident mass segregation for stars more massive than $10 M_{\odot}$, which accounts for the minor mass segregation found in the mass range of $1.00\text{--}12.14 M_{\odot}$ in this work. This suggests the overall mass segregation in Wd 1 is not primordial.

Keywords: Star Clusters (1567); Star Formation (1569); Star forming regions (1565); Stellar kinematics (1608)

1. INTRODUCTION

Young massive clusters (YMCs) are areas of intense star-forming activity and offer unique insight into star formation, cluster modeling, and the initial mass function (IMF) (Portegies Zwart et al. 2010). YMCs exist within disparate environments, ranging from the Galactic Center to the Galactic disk. Investigating differences in their physical properties allows us to determine the dependence of star formation on initial conditions. Finding similarities would indicate which fundamental mechanisms prevail despite such perturbations.

Westerlund 1 (Wd 1) is one of the most massive young star clusters in the Galaxy. Discovered more than a half-century ago (Westerlund 1961), Wd 1 is an ideal site to study a starburst environment in detail for its youth, proximity, and rich population of stars across a wide range of masses. Despite active studies, there remains substantial uncertainty about the distance and age of Wd 1, both of which are critical in accurately constraining the properties of cluster members.

Most previous studies have adopted a heliocentric distance of 4–5 kpc (e.g., Clark et al. 2005; Crowther et al. 2006; Kothes & Dougherty 2007; Gennaro et al. 2011;

Koumpia & Bonanos 2012; Rocha et al. 2022; Davies & Beasor 2019; Beasor et al. 2021; Navarete et al. 2022). On the other hand, Aghakhanloo et al. (2020) and Aghakhanloo et al. (2021) reported a much closer distance of $2.6_{-0.4}^{+0.6}$ kpc and $2.8_{-0.6}^{+0.7}$ kpc, respectively, from Gaia DR2 and EDR3 parallax measurements. The uncertainty in the distance leads to uncertainties in the mass and age of the cluster and thus limits our ability to understand the cluster’s evolution, such as the virial state of the cluster.

Previous studies have found a cluster age of 3–5 Myr, primarily derived from isochrone fitting of the cluster’s main sequence (MS) and pre-main sequence (PMS) stars, as well as from modeling the evolution of its massive stars (e.g., Clark et al. 2005; Crowther et al. 2006; Negueruela et al. 2010). However, growing evidence suggests that the lifetime of PMS stars is likely extended due to binary interactions, and may be longer than previously predicted (Eldridge et al. 2017; Beasor et al. 2019, 2021; Navarete et al. 2022). Beasor et al. (2021) reported an age of $10.4_{-1.2}^{+1.3}$ Myr using photometry of cool supergiants, and Navarete et al. (2022) derived 10.7 ± 1 Myr from the red supergiant spectra. Accurate measurements of the cluster age and distance from the CMD require modeling the kinematic and photometric membership and an extinction map.

As one of the most massive young clusters in the Milky Way, Wd 1 is a benchmark for testing models of star cluster formation and evolution. Due to the limited photometric depth of previous studies, the initial cluster mass of Wd 1 has been mostly derived by extrapolating a canonical IMF (Brandner et al. 2008; Clark et al. 2005; Andersen et al. 2017). This method suggested a cluster mass of $4 - 6 \times 10^4 M_{\odot}$, corresponding to a virial equilibrium velocity dispersion of $4 - 6 \text{ km s}^{-1}$. This estimate significantly exceeds the previously measured velocity dispersion of $2.1_{-0.9}^{+3.4} \text{ km s}^{-1}$ (Cottaar et al. 2012), implying that Wd 1 is subvirial and gravitationally bound, despite having dispersed most of its gas mass at an age of ~ 10 Myr. The virial state directly impacts these models, influencing assumptions about initial conditions, gas expulsion, and feedback in massive clusters.

Uncertainties about the virial state of Wd 1 persist due to the reliance on assumptions about its IMF. Currently, there are conflicting results on the high-mass slope of the IMF of Wd 1, e.g., $\alpha = -2.44_{-0.20}^{+0.08}$ in the mass range $3.5 - 27 M_{\odot}$ by Gennaro et al. (2011) and $\alpha = -1.8 \pm 0.1$ in the mass range $5 - 100 M_{\odot}$ by Lim et al. (2013). For low-mass stellar content, Andersen et al. (2017) argued for the IMF in the cluster to be consistent with the canonical IMF for the mass range $0.15 - 1.4 M_{\odot}$. Recent studies have reported similarly

unusual IMFs in other young massive clusters, such as the Galactic Center (Lu et al. 2013) and the Arches cluster (Hosek et al. 2019), raising the question of whether these deviations are driven by environmental factors or are intrinsic to young massive clusters in general. Wd 1 provides an excellent opportunity to test this. Kinematic membership is critical to remove the field star contamination, which could be high enough to inflate the slope of the IMF in the low-mass and substellar regimes.

Mass segregation in Westerlund 1 offers critical insights into the cluster’s dynamical evolution and star formation history. However, contradicting results have also been reported on the mass segregation in Wd 1. Gennaro et al. (2011) argued that the cluster appears mass-segregated, based on the radial variations of the IMF slope. Gennaro et al. (2017) later revisited the cluster using the mass segregation ratio Λ_{MSR} , and found little evidence of mass segregation for stars more massive than $3.5 M_{\odot}$, except for the most massive stars above $40 M_{\odot}$. The authors concluded that Wd 1 was not primordially segregated. The different result from (Gennaro et al. 2011) is attributed to fitting IMF slopes involving rather arbitrary binning, which could bias toward a high degree of mass segregation (Gennaro et al. 2017). Cottaar et al. (2012)

In this paper, we determine the kinematic and photometric cluster members of Wd 1 using observations with multiple epochs and filters from the Hubble Space Telescope (HST). With an extinction map based on the main-sequence population in the cluster, we present its differentially dereddened, field-decontaminated CMDs in the mass range $1.0 - 12.14 M_{\odot}$. We derive the radial profile of Wd 1 and examine the degree of mass segregation using the cluster members.

This paper is structured as follows. Section 2 illustrates the observation details. Section 3 introduces the extraction and calibration of the data. Section 4 elaborates on the methods we use for modeling the properties of the cluster, including determining cluster membership for each source, the extinction map, and completeness. In Section 5, we present the main results, including stellar density map, cluster morphology, radial profile, velocity dispersion, and mass segregation. We discuss the elongation, virial state, radial profile comparisons, dynamical timescales, the origin of mass segregation, and their implications in Section 6. Finally, we summarize the conclusions in Section 7.

2. OBSERVATIONS

Wd 1 (R. A. = $16^{\text{h}} 47^{\text{m}} 05.57^{\text{s}}$, Dec. = $-45^{\circ} 50' 24.14''$, J2000) was observed with the Hubble Space Telescope (HST) at multiple epochs to measure

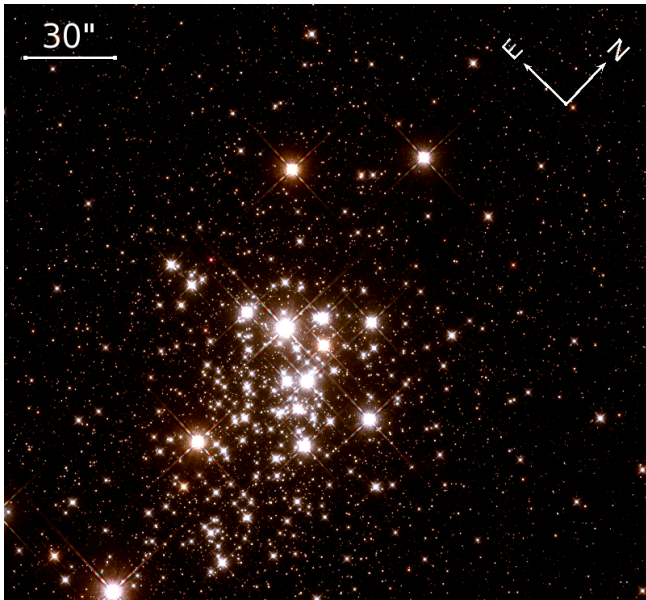


Figure 1. A Hubble Space Telescope WFC3-IR image of Westerlund 1 in false color. A logarithmic color stretch is used with red = F160W, green = F139M, and blue = F125W.

proper motions (PMs) and in multiple filters to obtain multi-color photometry. The cluster was observed at four different epochs — 2005, 2010, 2013, and 2015 — and in four filters at both red-optical and infrared wavelengths. See Figure 1 for a composite image.

The earliest data set was obtained on 2005 Jan 23 with the Advanced Camera for Surveys Wide Field Camera (ACS-WFC, GO-10172, [de Grijs 2004](#)) using the F814W filter ($\lambda = 806$ nm, $\Delta\lambda = 287$ nm). The total exposure time was 2407 seconds, comprised of 3 images with small dithers to cover the chip gap. The final image covers a $211'' \times 218''$ field of view (FOV). In these individual optical exposures, stars brighter than $m_{F814W} = 18.4$ were saturated; however, astrometry and photometry can still be extracted for stars as bright as $m_{F814W} = 13$ with increased uncertainty.

A second data set was obtained in 2010 with the infrared channel of the Wide Field Camera 3 (WFC3-IR) using three filters (GO-11708, [Andersen 2009](#)). Due to the limited FOV of WFC3-IR $\sim 130''$, a 2×2 mosaic was used to cover the entire 2005 ACS-WFC FOV. The three infrared filters were F125W ($\lambda = 1249$ nm, $\Delta\lambda = 285$ nm), F139M ($\lambda = 1384$ nm, $\Delta\lambda = 64$ nm), F160W ($\lambda = 1537$ nm, $\Delta\lambda = 268$ nm). Seven images per filter were observed at each point in the mosaic. The total exposure times for each tile were 2444 s in the F125W filter, 6294 s in the F139M filter, and 2094 s in the F160W filter, where each tile comprised 7 images.

A third and fourth data sets were obtained in 2013 (GO-13044, [Lu et al. 2016a](#)) and 2015 (GO-13809, [Lu](#)

[et al. 2016b](#)) with WFC3-IR in the F160W filter to provide multi-epoch astrometry for sources detected at infrared wavelengths. The position angle of the 2013 and 2015 WFC-IR data was rotated $\sim 180^\circ$ with respect to the position angle of the 2010 WFC3-IR data. Two short 8 s exposures were added to provide further information on the brightest stars in case the saturation and errors were unacceptable in the long exposures. Details of the exposure times, number of exposures, and sensitivity of each filter are presented in Table 1.

The data were reduced using the standard online HST data reduction pipeline and the resulting FLT images (`*.flt.fits`) were downloaded from the HST archive. All astrometric and photometric measurements were extracted from the individual FLT images and then combined as described in Section 3.1. The drizzle combined DRZ images (`*.drz.fits`) for each filter and epoch were used to calibrate the photometric zeropoints.

3. DATA ANALYSIS

3.1. Astrometric and Photometric Extraction

We construct an astrometric and photometric catalog for each HST data set as follows.

- i. Extract star lists of stellar positions and fluxes for each image
- ii. Cross-match star lists and transform them into a common astrometric reference frame
- iii. Combine astrometric and photometric measurements for all images within an epoch, in order to estimate average positions, fluxes, and associated errors.

The final product is a catalog for each epoch and filter of stellar fluxes in instrumental magnitudes and positions in pixels in a camera coordinate system. Instrumental fluxes are converted to Vega magnitudes as described in Section 3.2. Each step is described in more detail below.

First, stellar fluxes and positions are initially extracted from the individual `flt` images using point spread function (PSF)-fitting methods and the HST1PASS software adapted from [Anderson \(2022\)](#). During the source extraction process, the known camera distortions are corrected for both ACS-WFC and WFC3-IR¹ ([Anderson & King 2006](#)).

¹The WFC3-IR distortion solution can be downloaded from https://www.stsci.edu/files/live/sites/www/files/home/hst/instrumentation/wfc3/data-analysis/psf/_documents/STDGDC.WFC3IR.fits

Table 1. Wd 1 Observations from HST

Date ^a	Filter	P.A.	t_{exp} ^b	N_{img} ^c	N_{dith}	N_{stars}	σ_{trans}	HST ID
		(deg)	(s)				(mas)	
2005.485	F814W	46.43	802	3	1	10,056	0.30	11708
2010.652	F125W	-45.87	349	7	2×2	10,029	0.91	11708
2010.652	F139M	-45.87	899	7	2×2	10,028	0.92	11708
2010.652	F160W	-45.87	299	7	2×2	10,056	0.85	13044
2013.199	F160W	134.67	299	14	2×2	10,056	0.89	13044
2013.202 ^d	F160W	134.67	8	1	8×8	6,571	0.19	13044
2015.148	F160W	134.67	249	13	2×2	10,056	0.86	13809
2015.149 ^d	F160W	134.67	8	1	8×8	6,571	0.18	13809

^aImages were taken over the course of 2 days. The date used in the PM analysis is the average over the individual images.

^bExposure time for a single image.

^cNumber of images at each dither position.

^dThese data were sub-arrayed to one-quarter of the detector.

We derive the first-order coordinate transformations of all the star lists with HST1PASS, based on 2005 ACS-WFC F814W data as an initial reference frame, which has the finest resolution. Reference stars are chosen to fall within 0.07 ACS pixels or 3.5 mas and have an instrumental F814W magnitude between -13.5 and -10.0 . Uncertainties on positions and fluxes are derived from the root-mean-squared (RMS) error of the measurements in the individual exposures and are typically below 0.5 mas for the brightest stars. This process is repeated using the averaged star list from the first pass as a new reference frame and using more faint stars in the transformation. We note that the 2005 ACS-WFC F814W star list is also transformed to treat the two chips as independent images, each with its own transformation. This second pass reduces uncertainties by a factor of four to 0.006 ACS pixels, or 0.3 mas.

Preliminary PMs are determined by identifying cluster members, which are then used to establish a refined set of reference stars. The reference stars are selected based on the following properties:

- i. Preliminary PMs within 0.7 mas yr^{-1} of the cluster's mean motion;
- ii. Preliminary PM uncertainties less than 0.2 mas yr^{-1} ;
- iii. Photometric uncertainties of less than 5% in F814W and 10% in the IR passbands.

The entire process of transforming individual exposures is repeated with the new reference frame. The final

transformation residuals are listed in Table 1 for each epoch and filter.

With the image coordinate transformations in hand, we use the sophisticated source detection routine `ks2` (Anderson & King 2006; Anderson et al. 2008; Bellini et al. 2017, 2018) to extract stellar fluxes and positions from a stack of images, which results in a much deeper catalog. The positions and fluxes of these stars are measured from the individual image using the individual-image PSFs described earlier.

The positions of stars from each exposure are averaged within each epoch, and uncertainties of positions and fluxes are estimated in the same manner as described above. Figure 2 and Figure 3 show the final astrometric and photometric RMS errors, respectively, for all stars in the catalog.

3.2. Photometric Calibration

The final catalogs are photometrically re-calibrated since the published zeropoints for ACS-WFC and WFC3-IR are derived from aperture photometry rather than PSF fitting. We calculate a new photometric zero-point for each filter with the following procedure. First, we download the drizzle-combined mosaics from the HST archive and perform aperture photometry on the images using an aperture radius of $0''.4$ for the WFC3-IR images and $0''.5$ for the ACS images. The apparent magnitudes for the stars in the drizzled images were determined using the Space Telescope Science Institute's published 2012 photometric zeropoints with $R = 0.4$

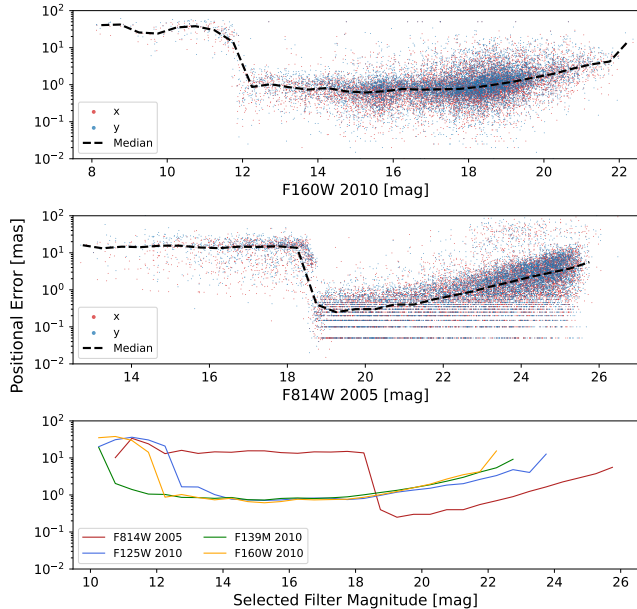


Figure 2. Astrometric error vs. brightness for all filters and years. The astrometric error is the RMS error over the individual exposures in each filter and epoch. The errors in x (red) and y (blue) are oriented along the detector coordinates of the 2005 F814W observations. The *dashed black* lines in the first two panels show the median error after rejecting outliers larger than 3σ . The *bottom panel* shows the median error line for all the filters and years.

aperture for WFC3-IR filters², and 2005 zeropoint for F814W³.

We cross-match stars between our final catalogs from *ks2* and the drizzled-image starlists. A set of photometric calibration stars is selected to be bright but not saturated in the instrumental magnitude range of -11.0 to -9.5 and to be isolated with no neighbors of comparable magnitudes within 0.25 mas. These stars are used to derive the average flux ratio and new zeropoints for our PSF photometry. Table 2 contains the zeropoints for both 2012 photometric calibration with $R = 0.4$ aperture and *ks2* photometry for all filters.

3.3. Final Proper Motions

PMs are derived with the linear fit on astrometric positions for stars detected in all of the four epochs including 2005 F814W, 2010 F160W, 2013 F160W, and 2015

² <https://www.stsci.edu/hst/instrumentation/wfc3/data-analysis/photometric-calibration/ir-photometric-calibration>

³ <https://acszeropoints.stsci.edu>

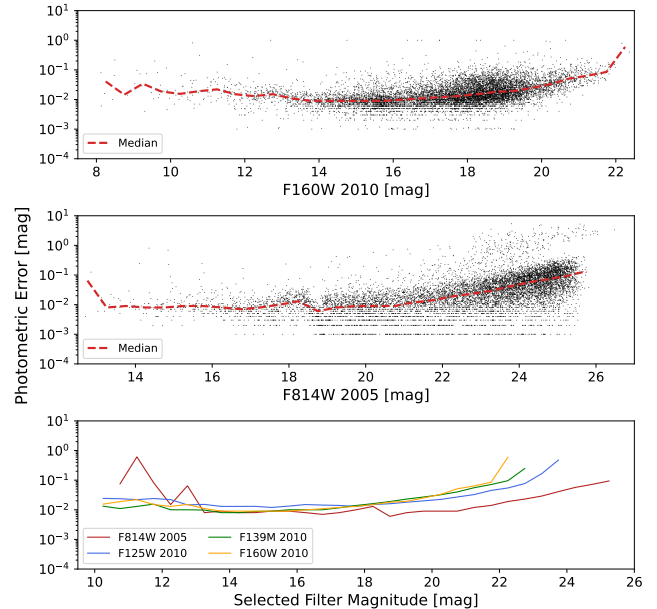


Figure 3. Photometric error vs. brightness for selected filters and years. The photometric error is the RMS error over the individual exposures in each filter and year. The *dashed red* lines in the first 2 panels show the median error after rejecting large ($> 3\sigma$) outliers. The *bottom panel* shows the optical and representative infrared filters/years.

Table 2. Photometric Zeropoints

Filter	Zeropoints (mag)	
	Aperture ^a	<i>ks2</i>
F814W	25.518	32.678 ± 0.010
F125W	25.144	25.231 ± 0.010
F139M	23.209	23.284 ± 0.010
F160W	24.504	24.570 ± 0.010

^a2005 zeropoint value for F814W and 2012 photometric calibration values $R = 0.4$ aperture for F125W, F139W, F160W.

F160W observations:

$$\alpha^* = \mu_{\alpha^*}(t - t_0) + \alpha_0^* \quad (1)$$

$$\delta = \mu_{\delta}(t - t_0) + \delta_0, \quad (2)$$

where t_0 is the average time weighted by the inverse square of the astrometric uncertainties, (α^*, δ) is the observed position at time t , and (α_0^*, δ_0) is the position at reference time t_0 . We adopt the flattened RA $\alpha^* = \alpha \cos \delta$ in this study. PMs are fit to the positions weighted by the inverse square of the positional

error in each epoch (see Ghez et al. 2005; Lu et al. 2009; Yelda et al. 2014; Hosek et al. 2015, for a more complete description). The resulting observed catalog contains 10,346 stars with PMs and associated uncertainties.

Rather than instituting a PM error cut on the resulting catalog, we opt to exclude stars with PMs exceeding 3σ from the median in both x and y directions (Figure 4). We institute the box cut to ensure that our membership selection process is not hampered by stars in the extreme edges of the PM distribution. This cut removes 344 stars from the catalog. The catalog contains 10,002 stars for the PM membership analysis.

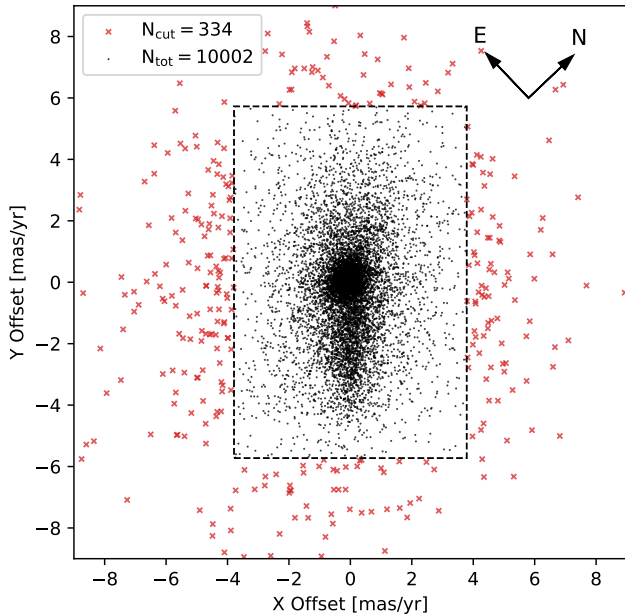


Figure 4. Proper motion vector point diagram of the entire catalog. The central box outlined by the black dashed lines shows the 3σ cut in both directions. The kept stars are marked in black points inside the box, and the cut stars are marked in red crosses outside the box.

4. METHODS

4.1. Cluster Membership

We distinguish cluster members from contaminating field stars by analyzing the PM distribution and CMD. Each star in the catalog is assigned a PM membership probability, p_μ , and a color membership probability according to its location in the CMD space, p_{color} . The PM membership p_μ is a continuous variable that ranges from 0 to 1, whereas p_{color} is a boolean criterion. The final membership value is the product of the two components, $p_{\text{clust}} = p_\mu \cdot p_{\text{color}}$. Only stars with $p_{\text{clust}} \geq 0.3$ are included in the structure and radial profile analysis.

First, we determine the PM membership. As cluster members tend to move with a systemic PM, they can be distinguished from the field populations kinematically and should form a compact region on the vector point diagram (VPD), a diagram showing the PM vectors in the x and y directions, respectively. To robustly identify the cluster members in the region, we adopt a Gaussian Mixture Model (GMM) to model the PM distribution of cluster and field stars with Bayesian inference. This model allows us to assign a kinematic cluster membership probability to each star based on its PM. The model employs a mixture of N Gaussians to represent the cluster and field star populations (see Clarkson et al. 2012; Hosek et al. 2015; Rui et al. 2019, for details), with N ranging from 2 to 5 explored in this analysis. We define the likelihood function for the set of N measured stars, \mathcal{L} :

$$\mathcal{L} = \prod_i^N L(\mu_i), \quad (3)$$

where $L(\mu_i)$ is the likelihood of the i -th star with a measured PM vector $\mu_i \equiv (\mu_{\alpha^*}, \mu_\delta)$, defined as:

$$L(\mu_i) = \sum_{k=0}^K \frac{\pi_k}{2\pi|\Sigma_{ki}|^{\frac{1}{2}}} \exp\left[-\frac{1}{2}(\mu_i - \bar{\mu}_k)^\top \Sigma_{ki}^{-1}(\mu_i - \bar{\mu}_k)\right] \quad (4)$$

for K Gaussian components, where π_k is the fraction of stars in the k -th Gaussian, $\bar{\mu}_k$ is the PM centroid vector of the k -th Gaussian, Σ_{ki} is the covariance matrix of the k -th Gaussian and the i -th star with a PM measurements of μ_i and an associated uncertainty of $\epsilon_i \equiv (\epsilon_{\alpha^*,i}, \epsilon_{\delta,i})$. Following Hosek et al. (2015) and Clarkson et al. (2012) we take

$$\Sigma_{ki} = S_i + Z_k, \quad (5)$$

where S_i is the diagonal components of the velocity error matrix

$$S_i = \begin{bmatrix} \epsilon_{\alpha^*,i}^2 & 0 \\ 0 & \epsilon_{\delta,i}^2 \end{bmatrix}, \quad (6)$$

and Z_k is the covariance matrix of the k -th Gaussian component:

$$Z_k = \begin{bmatrix} \sigma_{\alpha^*}^2 & \rho\sigma_{\alpha^*}\sigma_\delta \\ \rho\sigma_{\alpha^*}\sigma_\delta & \sigma_\delta^2 \end{bmatrix}. \quad (7)$$

Here $\sigma_{\alpha^*,i}$ and $\sigma_{\delta,i}$ denotes the intrinsic velocity dispersion in the right ascension and declination direction, and ρ denotes the correlation coefficient between the two components.

With the likelihood function, the posterior probability distribution is determined by the Bayes's theorem:

$$P(\pi, \bar{\mu}, \mathbf{Z} | \boldsymbol{\mu}, \mathbf{S}) = \frac{P(\boldsymbol{\mu}, \mathbf{S} | \pi, \bar{\mu}, \mathbf{Z}) P(\pi, \bar{\mu}, \mathbf{Z})}{P(\boldsymbol{\mu}, \mathbf{S})}, \quad (8)$$

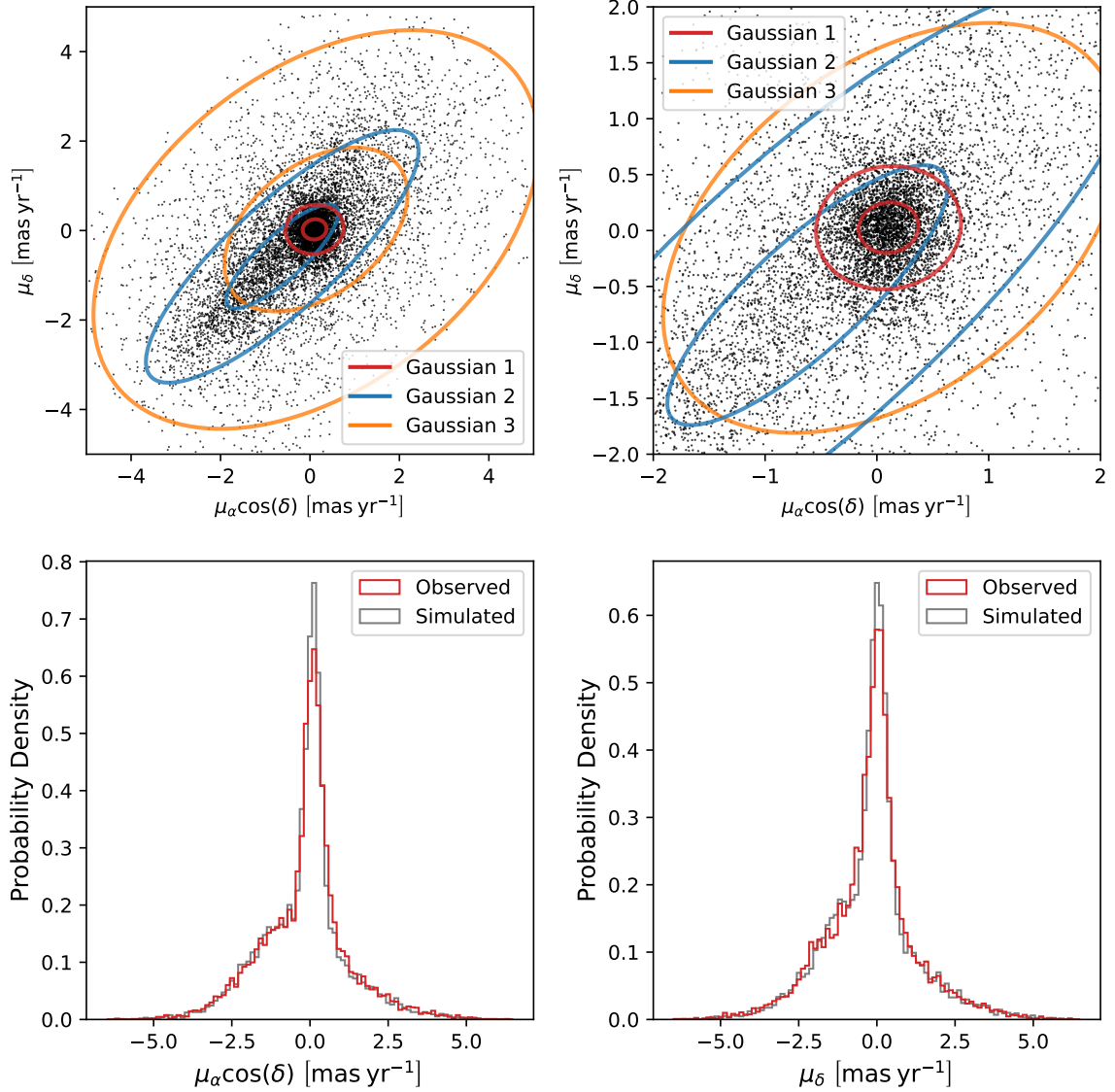


Figure 5. GMM fit and probability densities of the PMs. *Top:* Three-component GMM fit of the PMs shown in the *top left* panel and a zoomed-in view on the *top right* panel. Each Gaussian model is shown in its 1σ and 3σ iso-density ellipses. The first Gaussian depicted in red models the probability of being a cluster member, while the second and third Gaussian, shown in blue and amber, respectively, models the the field star probabilities. *Bottom:* Probability density distributions of PMs in the RA direction shown in the *bottom left* panel and DEC direction in the *bottom right* panel. Observed stars and simulated stars assuming the GMM perfectly describes their PM are shown in red and gray, respectively.

where $P(\boldsymbol{\pi}, \bar{\boldsymbol{\mu}}, \mathbf{Z} | \boldsymbol{\mu}, \mathbf{S})$ is the posterior probability of the model, $P(\boldsymbol{\mu}, \mathbf{S} | \boldsymbol{\pi}, \bar{\boldsymbol{\mu}}, \mathbf{Z})$ is the probability of the observed velocity distribution given the model, $P(\boldsymbol{\pi}, \bar{\boldsymbol{\mu}}, \mathbf{Z})$ is the prior probability of the model, and $P(\boldsymbol{\mu}, \mathbf{S})$ is the sample evidence. Here, $\boldsymbol{\pi}$ is the set of π_k values, $\bar{\boldsymbol{\mu}}$ the set of Gaussian velocity centroids, \mathbf{Z} is the set of Gaussian covariance matrices, $\boldsymbol{\mu}$ is the set of observed stellar PMs, and \mathbf{S} is the set of PM error matrices.

To fit the GMM, we use the `MultiNest` (Feroz et al. 2009), a multi-modal nested sampling algorithm, and its Python wrapper, `PyMultiNest` (Buchner et al. 2014).

To determine the merit of each K Gaussian model we compare the results of their Bayesian Inference Criterion (BIC) tests (Schwarz 1978). The BIC regularizes a model by modifying the fit residuals with a penalty for model complexity. We find the $N = 3$ model achieves the balance between describing the data well and the complexity of the model itself. The parameters, priors, and results are summarized in Table 3, and the Gaussians on the VPD are shown in Figure 5. We generate a simulated set of stars assuming the modeled GMM perfectly describes the PMs, and the comparison between

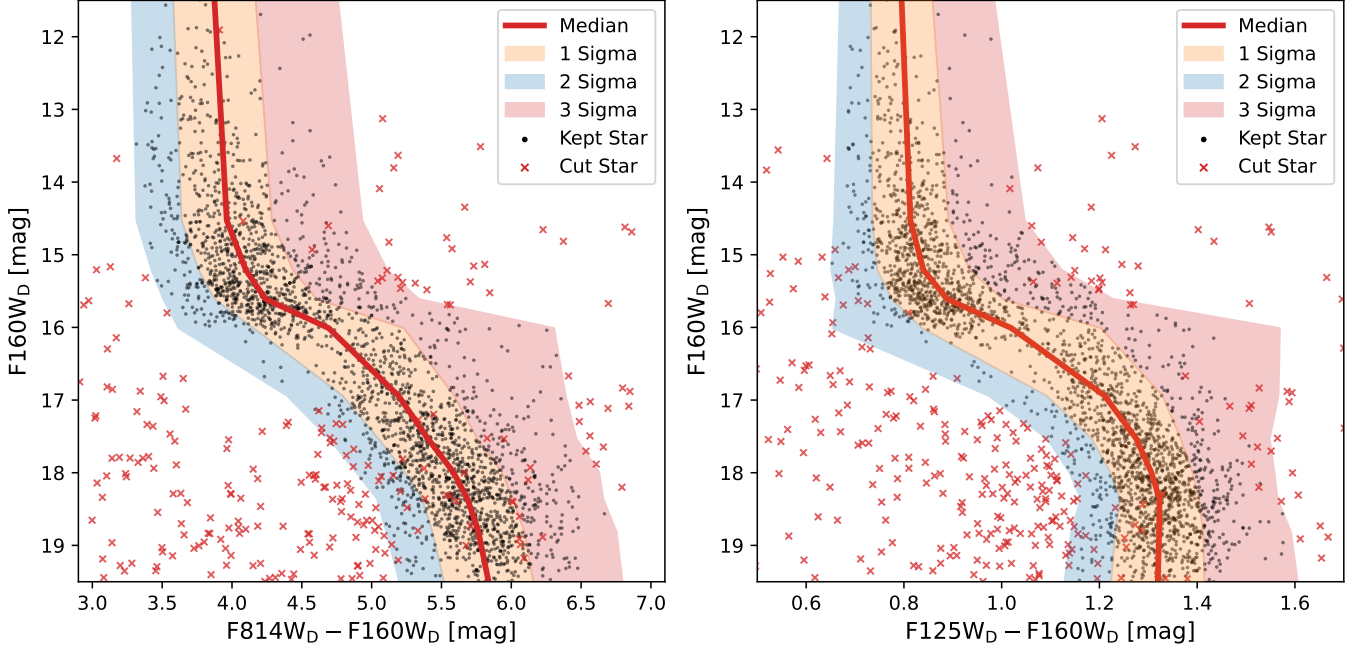


Figure 6. Color membership determination CMD’s for F814W–F160W (*left*) and F125–F160W (*right*). The yellow-shaded region represents 1- σ from the median. The blue and red shaded regions correspond to stars less than 2- σ bluer and 3- σ redder than the median, respectively. Stars 2- σ bluer or 3- σ redder than the median in each magnitude bin, or, equivalently, those outside any shaded regions, are excluded from our final analysis. Stars marked in red crosses are the cut stars, while black dots are the kept ones. Here the bins have been adaptively sized to contain approximately 287 stars in each of the 10 bins. Contaminating objects within our restricted cluster sequence may be binaries or field stars.

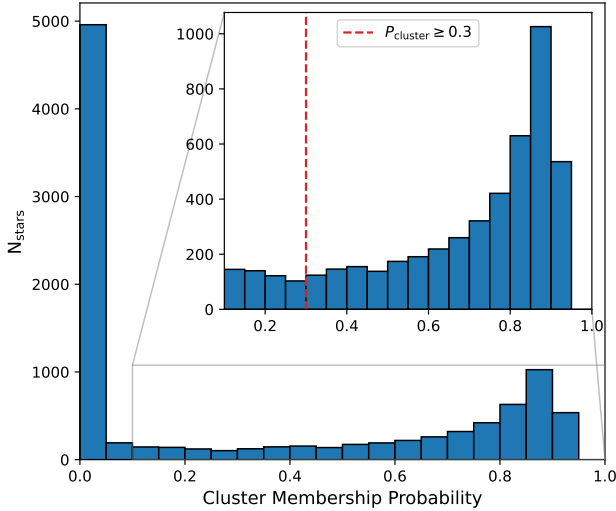


Figure 7. Histogram of the cluster membership probability $p_{\text{clust}} = p_{\mu} \cdot p_{\text{color}}$. The red dashed line in the inset figure marks the cluster membership limit of $p_{\text{clust}} = 0.3$.

the simulated and observed PMs are shown in the bottom panels in Figure 5. Note that the GMM modeling of the VPD is consistent across magnitudes and that there is no benefit in performing the magnitude-by-magnitude GMM modeling with this dataset.

With the GMM model, the PM membership probability p_{μ}^i is determined as:

$$p_{\mu}^i = \frac{\pi_1 P_1^i}{\sum_{k=1}^3 \pi_k P_k^i}, \quad (9)$$

where π_k is the normalized fraction of the k -th Gaussian, and P_k^i is the probability of the i -th star being in the k -th Gaussian.

Next, we determine the color membership. Since cluster members are assumed to have the same age, distance, and metallicity, they are expected to follow a distinct sequence in CMD space. Thus, we can eliminate stars with photometry inconsistent with the cluster sequence as likely field contaminants. Applying color cuts thus further reduces field contamination. After masking the low-completeness region, we select stars with high kinematic membership probabilities with $p_{\mu}^i \geq 0.7$, and determine the median and standard deviation of colors in differentially dereddened magnitude bins each containing 287 stars. We will illustrate the dereddening and completeness in Section 4.3 and Section 4.2, respectively. Figure 6 shows the color-magnitude diagram with our 1-, 2-, and 3- σ masks in F160_D vs. F814W_D – F160W_D and F160_D vs. F125W_D – F160W_D spaces. Stars bluer

Table 3. Kinematic Membership Gaussian Mixture Model: Parameters, Priors, and Results

Parameters	Unit	Cluster Gaussian		Field Gaussian 1		Field Gaussian 2	
		Prior ^a	Result	Prior	Result	Prior	Result
π_k	...	$U(0, 1)$	0.33 ± 0.01	$U(0, 1)$	0.34 ± 0.01	$U(0, 1)$	0.33 ± 0.01
$\mu_{\alpha^*, k}$	mas yr^{-1}	$\mathcal{N}(0, 0.3)$	-0.05 ± 0.01	$U(-10, 10)$	0.01 ± 0.02	$U(-10, 10)$	-0.08 ± 0.04
$\mu_{\delta, k}$	mas yr^{-1}	$\mathcal{N}(0, 0.3)$	0.09 ± 0.01	$U(-10, 10)$	-0.85 ± 0.07	$U(-10, 10)$	0.11 ± 0.08
σ_k	mas yr^{-1}	$U(0, 1)$	0.27 ± 0.01	$U(0, 8)$	1.64 ± 0.05	$U(0, 8)$	2.33 ± 0.05
ϵ_k	...	$U(0, 1)$	0.84 ± 0.04	$U(0, 1)$	0.30 ± 0.02	$U(0, 1)$	0.62 ± 0.02
θ_k	rad	$U(0, \pi)$	0.99 ± 0.15	$U(0, \pi)$	1.55 ± 0.02	$U(0, \pi)$	1.47 ± 0.03

NOTE—Parameter description: π_k : normalized fraction of the k -th Gaussian. $\mu_{\alpha^*, k}$, $\mu_{\delta, k}$: Mean proper motion of the k -th Gaussian in α^* and δ . σ_k : Standard deviation of the k -th Gaussian in the semi-major axis direction. ϵ_k : Semi-minor to semi-major axis ratio, or ellipticity of the k -th Gaussian. θ_k : Rotation angle of the semi-major axis of the Gaussian ellipse from the positive- x direction.

^a $U(a, b)$ stands for uniform distribution between a and b , and $\mathcal{N}(\mu, \sigma)$ denotes normal distribution with a mean of μ and standard deviation of σ .

than 2σ or redder than 3σ than the bulk cluster in either CMD space are assigned $p_{\text{color}} = 0$, otherwise $p_{\text{color}} = 1$. We adopted a stricter cut on the blue side because some fraction of cluster members might be expected to have extra intrinsic reddening from circumstellar disks given that the youth of the cluster.

The final membership p_{clust} is then the product of p_{μ} and p_{color} . We require $p_{\text{clust}} \geq 0.3$ to be used in our analysis, resulting in a catalog of 3586 unweighted stars. A histogram of the resulting probabilities is shown in Figure 7.

4.2. Extinction

As reddening is a function of position, we correct for extinction by producing a spatial attenuation map and differentially deredden the stars in our catalog. In the following analysis, we use the subscript D after the filter names to denote the dereddened magnitude. We create an extinction map for the field based on individual extinction values derived for high-probability main-sequence cluster members. The intrinsic colors of such stars are nearly independent of mass in the NIR filters, and so their extinction can be estimated from their observed color given an assumed distance and extinction law.

To determine the attenuation value A_{K_s} , we produce a series of PARSEC (Bressan et al. 2012) isochrones with a distance of 3077 pc, age of 10.7 Myr, and solar metallicity, which were determined to be the best-fit model values by inspection and are consistent with literature values (e.g., Beasor et al. 2021; Navarete et al. 2022). We then varied the cluster extinction A_{K_s} value using the revised extinction law of Hosek et al. (2019). This law has

been derived using stars from the Arches and Wd 1 for optical and near-infrared (NIR) extinction in highly reddened regions. We find an isochrone with $A_{K_s} = 0.73$ to perform best for both the optical and NIR filters. We produce a secondary isochrone with the same attributes but with an attenuation of $A_{K_s} = 1.03$, 0.3 more than the reference isochrone to calculate the slope of the shift of a star’s position in the CMD, or the reddening vector, with a change in extinction.

We produce a pixel-by-pixel reddening map by utilizing high kinematic membership probability ($p_{\text{clust}} \geq 0.7$) main-sequence (MS) stars brighter than F160W = 15.0 mag, which is 0.5 mag brighter than the PMS turn-on. We interpolate along mass in each isochrone and map reddening vectors as a function of mass between the fiducial and secondary isochrones. Each star is assigned an extinction value based on the distance from the reference isochrone along the nearest reddening vector. We reject stars with A_{K_s} values further than 3σ away from the mean A_{K_s} , as well as stars with a distance further than 0.25 mag from the nearest reddening vector on the CMD. After the rejection, we are left with 447 stars out of 2934 for assigning extinction values, with a median $A_{K_s} = 0.78 \pm 0.06$ mag.

We assign each pixel an extinction value and error via the 3σ clipped mean of the 30 nearest neighbors among the 447 stars used to calculate extinction. The resulting IR extinction map is shown in Figure 9. The extinction error map (σ_{map}) is calculated as $\sigma_{A_{K_s}} / \sqrt{N}$, where $\sigma_{A_{K_s}}$ is standard deviation of the extinction values and N is the number of stars used. Stars in the catalog are assigned the extinction and error of the pixel they fall

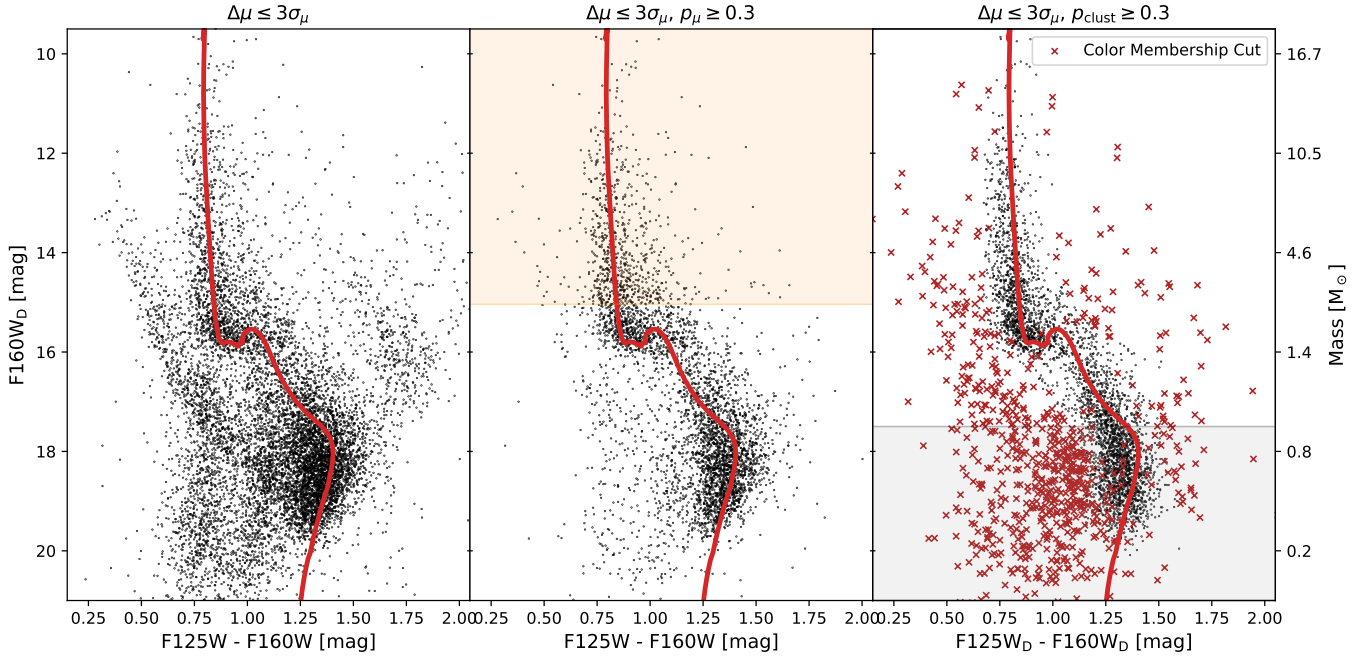


Figure 8. *Left:* CMD of the cluster catalog after applying a $3\sigma_\mu$ box cut in the x and y directions. *Center:* CMD of cluster PM membership $p_\mu \geq 0.3$ and reference isochrone with an A_{K_s} of 0.73 mags, distance of 3077 pc and age of 10.7 Myr. The *orange shaded* region indicates the faintest dereddened magnitude limit of 15.04 F160W_D of the stars used to produce the extinction map. *Right:* CMD of cluster members with $p_{\text{clust}} \geq 0.3$ after extinction correction and color membership cut, with rejected stars marked with *red x's*. The *gray shaded* region corresponds to stars fainter than our completeness cut of 17.5 mag.

on. We build separate extinction maps from the optical and IR photometry to see which one results in a tighter cluster on the CMD.

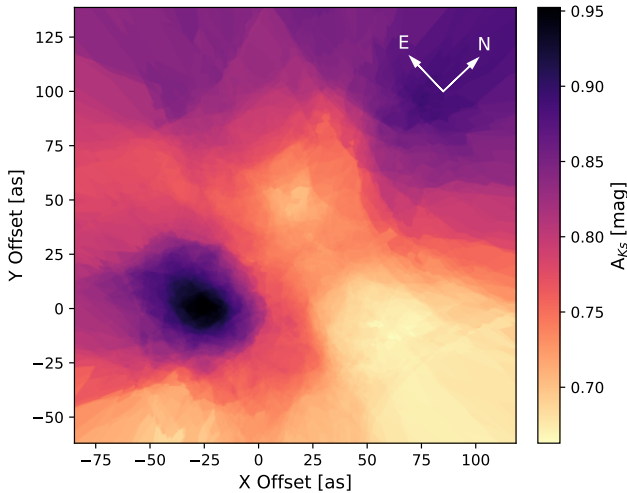


Figure 9. IR extinction map produced by analysis of the extinction values of the MS stars. The map axes are referenced to the non-completeness corrected centroid of the cluster, weighted by the dereddened F160W magnitudes. The assigned pixel values are taken from the mean of the 30-nearest 3σ clipped stars.

Optical and NIR extinction maps are remarkably consistent as our assumed extinction law is consistent across the wavelengths. Both maps show significant spatial variability over a similar range of extinction values, with $\Delta A_{K_s} = 0.27$ mags for the optical CMD-based map and $\Delta A_{K_s} = 0.29$ mags for the IR CMD-based map. The median of both maps is $A_{K_s} = 0.79 \pm 0.06$ mags, with the error being the standard deviation of the map. The maps can differ by as much as $|A_{K_s}| = 0.04$ mag with a median absolute difference of $A_{K_s} = 0.005$ mag. In addition, the pixel value errors on the IR CMD-based map are just slightly lower, with a median error of $A_{K_s} = 0.013$ mag versus $A_{K_s} = 0.014$ mag for the optical CMD-based map. The maximum absolute difference between the pixel value errors of the two maps is 0.013 mag.

Our extinction maps are consistent with the observations of Brandner et al. (2008), in which the authors claimed that the regions east and north of the cluster center tend to have slightly higher extinctions, while the regions west and south of the cluster have slightly lower extinction. Lim et al. (2013) also found the east side of the field to have higher extinction than the west side, though they also observed the highest reddening towards the cluster center. In our extinction maps, a relatively high patch of reddening is found to the south-east of the uncorrected cluster center. The cause of this

discrepancy is likely due to the smaller sample size of Lim et al. (2013), who measured the reddening of 53 OB supergiants. Our reddening sample is much larger, allowing us to map out the differential reddening in more detail.

The differentially dereddened CMD is shown in the right panel of Figure 8. In this work, we adopted the IR extinction map in F125W, shown in Figure 9.

4.3. Completeness

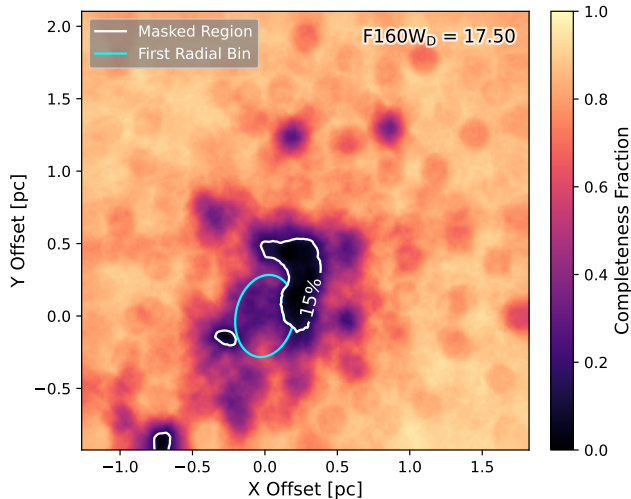


Figure 10. 2D completeness map for dereddened F160W_D mag of 17.5. The white contours show the 15% low completeness regions which are masked in the radial profile analysis. The partial *cyan ellipse* shows the inner-most radial bin for completeness check with an effective radius of 0.29 pc.

As the region is crowded, completeness correction is vital to account for the unobserved stars contaminated by the bright stars. We estimate the completeness of our final catalog by planting a set of artificial stars into the original images and processing them through our entire analysis pipeline. The procedure for this analysis has been described in detail in earlier work (Lu et al. 2013; Hosek et al. 2015, 2019; Rui et al. 2019) and entails planting and extracting 600,000 artificial stars. The positions of the artificial stars are randomly sampled from a uniform distribution over the FOV. The fluxes of the artificial stars are generated to thoroughly cover the color-magnitude space populated by the observed stars with some additional padding on all sides.

We modify the astrometric and photometric errors of the detected artificial stars to incorporate additional systematic uncertainties, potentially arising from PSF variability, intra-pixel sensitivity variations, and uncorrected residual distortions in the simulations (Hosek et al. 2015). The systematic error terms are then added

in quadrature, ensuring that the resulting error distributions at different magnitudes for the simulated stars match that of the observed stars.

Artificial stars are matched across all filters and epochs, and their PMs are fit in the same manner as the observed data. We note that, after accounting for systematic errors in the observed stars, the final distribution of PM errors for the artificial stars matches the observed stars. There are 423,790 out of 600,000 stars detected in all four epochs: 2005 F814W, 2010 F160W, 2013 F160W and 2015 F160W. This catalog is used to construct a spatial completeness map and completeness curves as a function of magnitude.

To construct the completeness map, we first produce a grid of reference points of 1 as-by-1 as in x and y directions. We determine the completeness of each reference point from their nearest 2000 neighbors in each filter and each magnitude bin ranging from 8–32 mags with a step size of 0.5 mag. Each reference pixel is assigned a completeness value for each magnitude bin. Observed stars are then assigned the completeness value of the nearest reference point.

We mask the regions affected by low completeness smaller than 15% at F160W_D = 17.5, or equivalently $1.0 M_{\odot}$, as shown in the white contours in Figure 10. The partial *cyan ellipse* is the inner-most radial bin in the remaining image with an effective radius of 0.29 pc used in the radial profile analysis in Section 5.2, which has the lowest completeness. The size, orientation, and elongation of the ellipse are modeled by a 2D Gaussian profile fit to the stellar densities, which will be discussed in Section 5.1. It only serves as a test on the lowest completeness region.

To check the completeness of the remaining field, we first construct the 1D completeness curves by interpolating along the magnitudes for all of the remaining fields and for the central low completeness region, as shown in Figure 11. As can be seen from the completeness curves in the right panel in Figure 11, cutting the stars fainter than F160W_D = 17.5 is equivalent to applying a 65% completeness limit in the inner-most radial bin.

Furthermore, we check the independence of the field stellar density on the effective radius, as is expected for a small FOV in our observation. For this purpose, we interpolate the completeness for each star only as a function of the effective radius and magnitude, instead of using the pixel completeness calculated as in Figure 10. Note that the interpolated completeness is only used to check the field stellar density, and the pixel completeness is used for the actual analysis. We use 2D interpolation on a magnitude grid ranging from 10 to 22 mag in F160W_D with a step size of 0.5 mag, and on the 10

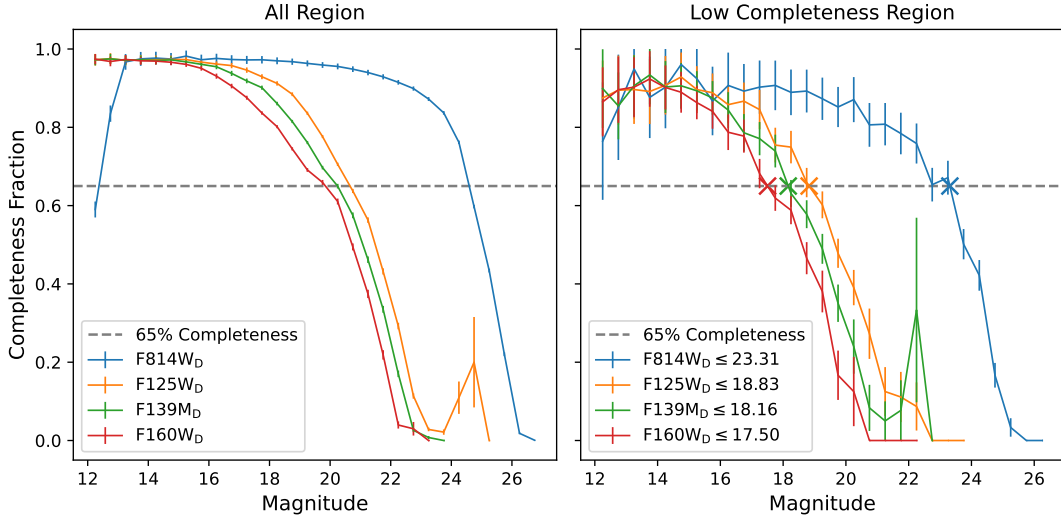


Figure 11. *Left:* 1D completeness curves for the entire field. *Right:* 1D completeness curves for the low completeness region marked in Figure 10. The *gray dotted* line in each plot marks the 65% completeness limit. After masking out the lowest 15% completeness regions, our cut at 17.5 mag in dereddened F160W_D is equivalent to a 65% completeness limit in the low completeness region.

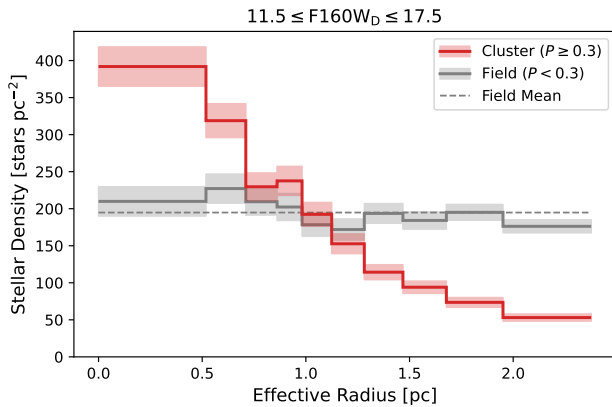


Figure 12. Dependence of completeness-corrected cluster and field stellar densities on effective radius using interpolated completeness as a function of effective radius and magnitude. The cluster members with $p_{\text{clust}} \geq 0.3$ are shown in *red*, and the field stellar density with $p_{\text{clust}} < 0.3$ is shown in *gray*. The *dashed gray* line represents the mean field stellar density across the effective radius.

radial bins which equally partition the corrected stellar count. The resulting cluster and field stellar densities as a function of effective radius after correcting for membership, completeness, and area fraction are shown in Figure 12. To confirm the independence of the field

stellar density on effective radius after completeness correction, we performed a Kolmogorov–Smirnov (KS) test on 10,000 simulated field stellar density arrays of length 10, same as the length of radial bins in Figure 12, with each element following a normal distribution centered at the measured value and a standard deviation being the associated uncertainty in that bin. The simulated data is tested against a normal distribution with the expectation being the mean of the measured field stellar density across the effective radius, and the standard deviation being the standard deviation of 10 measured field stellar densities. The null hypothesis is that the field stellar density in each bin follows the same Gaussian distribution independent of the effective radius. The resulting p -value of the 10,000 simulations is 0.49 ± 0.27 , significantly greater than the critical value of 0.05. Therefore, we cannot reject the null hypothesis, verifying the uniform distribution of field stars. The independence of field stellar density on effective radius proves the reliability of our completeness correction.

5. RESULTS

We present the full cluster catalog with PMs, dereddened magnitudes, kinematic and color membership probabilities, and completeness values of each star in Table 4.

Table 4. Summary of Structural and Kinematic Properties for Wd 1

ID	F814W _D mag	F125W _D mag	F160W _D mag	$\Delta\alpha_0^a$ as	$\Delta\delta_0$ as	μ_{α^*} mas yr ⁻¹	μ_δ mas yr ⁻¹	t_0 year	p_μ	p_{color}	p_{clust}	C	M M_\odot	r_{eff} pc	$f(r_{\text{eff}})$
wd1 00001	18.57	15.20	14.30	-29.23	-17.95	-0.49 ± 0.14	-0.19 ± 0.15	2011.698	0.30	1	0.30	0.97 ± 0.21	3.96	0.55	0.87
wd1 00002	18.98	15.46	14.52	-53.22	66.76	0.53 ± 0.04	0.35 ± 0.04	2010.997	0.59	1	0.59	0.97 ± 0.18	3.59	1.78	0.61
wd1 00003	17.58	14.59	13.84	2.99	149.76	-0.01 ± 0.05	0.21 ± 0.04	2009.482	0.89	1	0.89	1.00 ± 0.19	4.89	2.56	0.18
wd1 00004	18.58	15.31	14.46	98.69	26.38	0.06 ± 0.02	0.10 ± 0.02	2008.278	0.92	1	0.92	0.99 ± 0.18	3.69	1.82	0.57
wd1 00005	19.52	15.81	14.85	40.75	61.88	0.10 ± 0.04	0.25 ± 0.04	2009.879	0.90	1	0.90	0.97 ± 0.16	3.08	1.11	0.82
...

NOTE—Description of columns: *ID*: Star name. *F814W_D*, *F125W_D*, *F160W_D*: mags in corresponding filters (Vega). $\Delta\alpha_0^*$, $\Delta\delta_0$: Relative position in α^* and δ at time t_0 . t_0 : Average observation time weighted by the inverse of astrometric uncertainties. p_μ : Proper motion membership. p_{color} : Color membership. p_{clust} : Product of proper motion membership and color membership. C : Completeness. M : Stellar mass. r_{eff} : Effective radius. $f(r_{\text{eff}})$: Area fraction.

^aPositions are relative to RA = 16^h47^m04.0^s, DEC = -45°51'04.7" (J2000).
(This table is available in its entirety in machine-readable form)

5.1. Stellar Density And Morphology

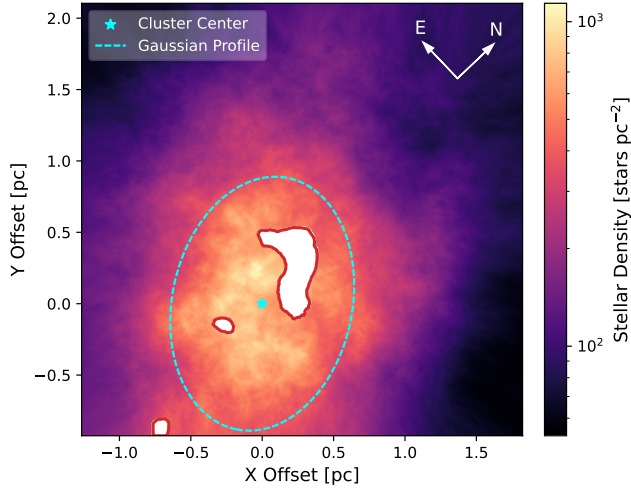


Figure 13. Stellar density map corrected by membership probability and completeness for stars with $p_{\text{clust}} \geq 0.3$ and $F160W_D$ between 11.5 and 17.5 mag. The cyan star and dashed ellipse indicate the cluster center and the best-fit Gaussian profile, respectively. Note that the centroid has shifted to the lower left, or south. This is due to the large extinction values in that area being accounted for in this map.

We calculate the 2D stellar density map of stars with $p_{\text{clust}} \geq 0.3$ and $F160W_D$ between 11.5 and 17.5 mag with membership and completeness correction. This results in an uncorrected star count of $N = 1951$. Each star is weighted by:

$$w_i = \frac{p_\mu^i}{C_i}, \quad (10)$$

where p_μ^i is the PM membership of the i -th star, and C_i is the completeness value of the nearest reference pixel and appropriate magnitude bin used for each star. The stellar density map is derived by the weighted stellar density within the radius of the 50th nearest neighbor for each pixel. Specifically, it is calculated as the sum of the weighted stellar counts divided by the overlapping area between the circle centered on the pixel and the masked image.

To determine the morphology of Wd 1 including its orientation, centroid, and elongation, we fit a 2D Gaussian profile to the completeness-corrected stellar density map. Throughout this work, we adopt the center of the Gaussian density profile as the Wd 1 center, located at $\text{RA} = 16^{\text{h}}47^{\text{m}}04.0^{\text{s}}$, $\text{DEC} = -45^\circ51'04.7''$ (J2000). We find that the cluster is elongated in a northeast-southwest direction, with the semi-major axis at a position angle of $\sim 56^\circ$ east of north. This aligns the elonga-

tion with the Galactic plane and cluster PM movement spread, as seen in Figure 5. The flattening or ellipticity of the Gaussian profile ϵ , defined as the ratio of the semi-minor to the semi-major axis, is approximately 0.70, translating to an eccentricity of $e = \sqrt{1 - \epsilon^2} = 0.71$.

The stellar density map and the Gaussian profile of the full catalog and three mass bins are shown in Figure 13 and Figure 14, respectively. The cyan star represents the cluster center, and the dashed ellipse marks the $1-\sigma$ contour of the 2D Gaussian density profile. Both figures adopt the log-scale colormap. The elongation and its direction can be observed from Figure 13. The shrink in radius with increasing mass is clearly visible in Figure 14 under identical colormap for each mass bin, indicating the massive stars are more concentrated in the center.

5.2. Radial Profile

To measure the radial profile that accounts for the edge effect of our limited FOV, we introduce the concept of an area fraction $a(r_{\text{eff}})$ for an annulus centered at the cluster center with an effective radius r_{eff} and thickness dr_{eff} . The area fraction adjusts for the incomplete coverage near the edges and quantifies the proportion of the annular area that overlaps with our FOV. Specifically, it is defined as the ratio of the overlapping area between the annulus and the completeness-masked image to the total area of the annulus assuming an infinite FOV:

$$f(r_{\text{eff}}) = \frac{A_{\text{overlap}}(r_{\text{eff}})}{A_{\text{total}}(r_{\text{eff}})}, \quad (11)$$

where $A_{\text{overlap}}(r_{\text{eff}})$ is the overlapping area and $A_{\text{total}}(r_{\text{eff}}) = 2\pi r_{\text{eff}} dr_{\text{eff}}$ is the total area of the annulus. We interpolate the area fraction in each 1-pixel-wide annuli centered on the Gaussian profile center as a function of the effective radius. Each star is then weighted by $w_i^{r_{\text{eff}}}$ to determine the radial profile:

$$w_i^{r_{\text{eff}}} = \frac{1}{f(r_{\text{eff}})} \frac{p_\mu^i}{C_i}. \quad (12)$$

This weight is only used in radial profile modeling. To prevent amplifying the weights beyond reasonable levels, we cautiously restrict the area fraction $f(r_{\text{eff}}) \geq 0.3$. Together with the completeness magnitude cut at $F160D \leq 17.50$, or equivalently $M \geq 1.00M_\odot$, we end up with a maximum effective radius of 2.38 pc. The resulting catalog has 1885 uncorrected stars, or 2404.9 weighted stars.

Next, we fit the radial profile to an Elson, Fall, and Freeman model (Elson et al. 1987, EFF hereafter), which has been found to be a good description of other young clusters (Mackey & Gilmore 2003a,b; McLaughlin & van der Marel 2005; Rui et al. 2019; Hosek et al. 2015) as

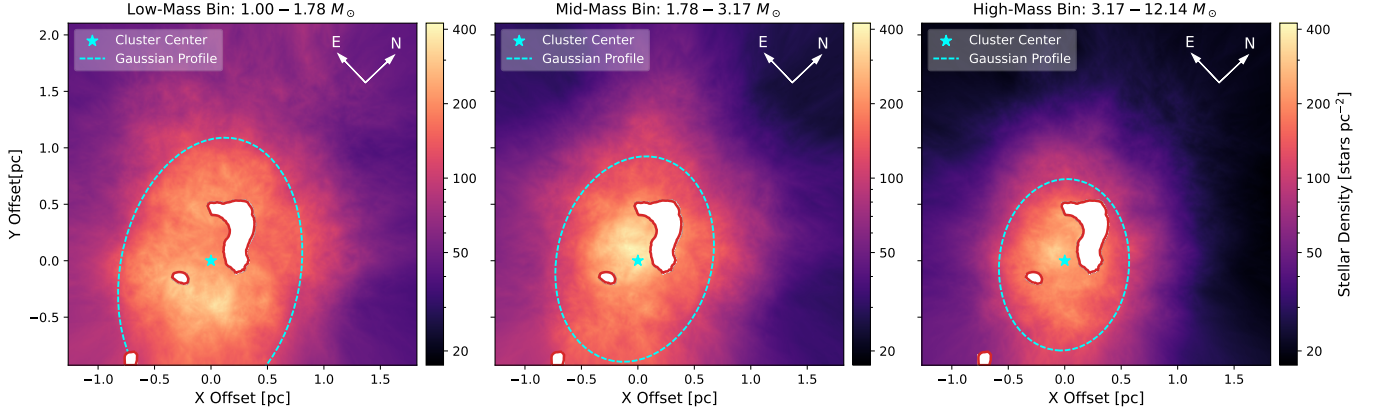


Figure 14. Stellar density map for increasing mass bins. The mass range of each bin is $1.00\text{--}1.78 M_{\odot}$, $1.78\text{--}3.17 M_{\odot}$, and $3.17\text{--}12.14 M_{\odot}$, from left to right respectively. The cyan star marks the center of the full cluster, and the dashed ellipse shows the Gaussian profile for each individual mass bin. Note that the colormap used in each panel is in log-scale and consistent.

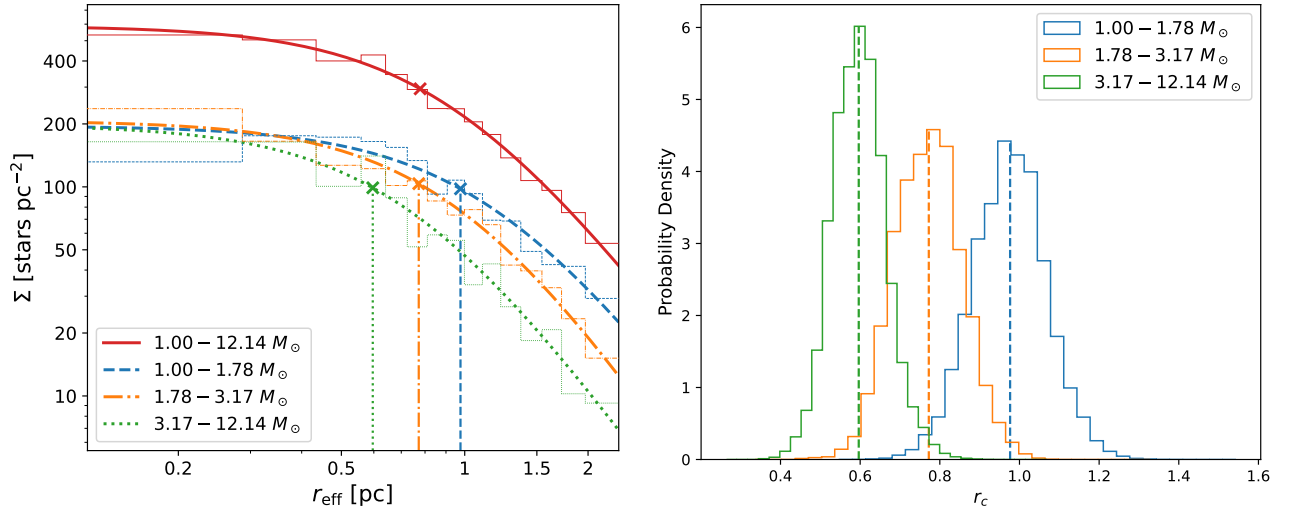


Figure 15. *Left:* Binned radial profile and EFF model in each mass bin. The binned radial profile is represented as the stair plots, and the EFF model is shown as the curves. The width of each stair corresponds to the bin r_{eff} range, and the shaded region represents the Poisson uncertainty. Bins were chosen to have an equal number of stars weighted by w_i^r with the area fraction $f > 0.30$, which corresponds to $r_{\text{eff}} < 2.38$ pc. *Right:* Posterior distributions of r_c with the median value marked with a dashed line.

well as Wd 1 (Gennaro et al. 2011; Andersen et al. 2017). The EFF profile takes the form:

$$\Sigma(r) = \Sigma_0 \left(1 + \frac{r^2}{a^2} \right)^{-\gamma/2} \quad (13)$$

where Σ_0 is the amplitude, r is the radius, a is the core parameter, and γ is the slope of the power law. We assume our background contamination is zero, as the radial range explored in this work is insufficient to constrain the parameter accurately. The background contamination parameter is not constrained if included, and affects the convergence of other parameters as well due to degeneracies in the parameter space. The core pa-

rameter a is related to core radius r_c of the cluster by:

$$r_c = \frac{a}{\sqrt{2^{\gamma/2} - 1}}. \quad (14)$$

Note that we only model r_c , and the posterior of a is purely converted from r_c and shown for illustration purposes. Due to the eccentricity of Wd 1, we de-rotate the image to align the semi-major axis of the Gaussian profile to the y direction and rescale the x pixel coordinates by a factor of $1/\epsilon$. This transforms the elliptical Gaussian profile into a circular one in the new coordinates. The r in the EFF profile is therefore replaced by an effective radius r_{eff} :

$$r_{\text{eff}} = \sqrt{(x'/\epsilon)^2 + y^2} \quad (15)$$

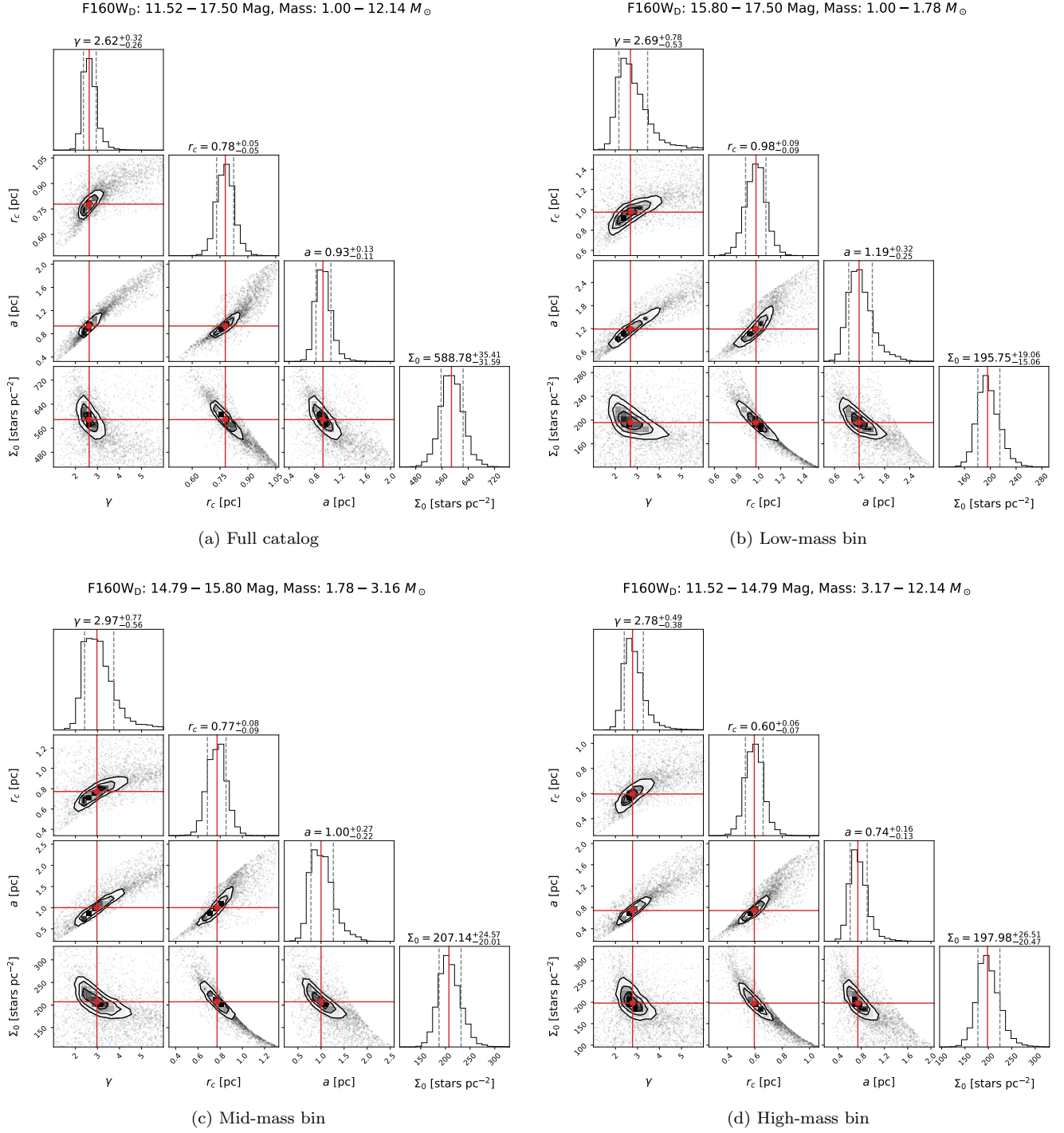


Figure 16. Weighted posterior distributions of EFF radial profile parameters. (a): Full catalog. (b): Low-mass bin. (c): Mid-mass bin. (d): High-mass bin. The red lines mark the weighted median, and the gray dashed line marks the weighted 16- and 84-th percentiles. Note that we only modeled r_c , and the posterior distribution of a is purely converted from r_c .

where x' and y' are the de-rotated coordinates.

To perform the EFF fit, we use `MultiNest` to maximize the log-likelihood function:

$$\log \mathcal{L} = \sum_{i=1}^N w_i \log \Sigma(r) \quad (16)$$

where N is the number of stars used for the fit, w_i the aforementioned weight of each star, and $\Sigma(r)$ is the EFF model. We refer to [Richardson et al. \(2011\)](#) and [Cicúendez et al. \(2018\)](#) for the derivation and further discussion of the log-likelihood function and [Do et al.](#)

(2013) and Hosek et al. (2015) for further discussion of the methodology.

We derive the best-fit models based on the entire catalog and divide the full sample into 3 mass bins with a total weight ratio of roughly 4 : 3 : 2 from the lowest to highest mass to explore the difference in radial density for each mass bin.

Figure 15 shows the best-fit EFF model and the measured radial profiles in 15 radial bins that share the same center, orientation, and elongation with the Gaussian density profile and contains an equal number of weighted sources. It is worth mentioning that the observed values represented as the stair plot in Figure 15 are calculated as the sum of weights defined in Equation 10 divided by the actual area of each bin, which allows a more accurate representation of density in each bin. The area fraction-corrected weight in Equation 12 is only used in EFF profile modeling. The posteriors of the EFF radial profile fits are shown in Figure 16 for the full and 3 binned catalogs. The aforementioned low completeness region in Figure 10 is the innermost radial bin.

The results of the EFF profile model parameters are summarized in Table 6, including the comparison with the Arches and Quintuplet cluster that will be discussed in Section 6.3. We find the core radius r_c for the full cluster ($p_{\text{clust}} \geq 0.3$, $11.52 < \text{F160W}_D < 17.50$, and $r_{\text{eff}} \leq 2.38$ pc) to be 0.78 ± 0.05 pc, and the r_c decreases with increasing mass, which is an indication of mass segregation: higher mass stars tend to be more concentrated in the center.

5.3. Velocity Dispersion

We model the intrinsic PM velocity dispersion for the subsample by a mixture of two bivariate Gaussians, one for the cluster members (subscripted by cl) and the other for the residual foreground stars (subscripted by fg). Each Gaussian is characterized by the mean PM values $\bar{\boldsymbol{\mu}} \equiv (\bar{\mu}_R, \bar{\mu}_T)$, the PM dispersions $\boldsymbol{\sigma} \equiv (\sigma_R, \sigma_T)$, and the correlation coefficient ρ . Given a set of PM measurements $D \equiv \{\boldsymbol{\mu}_i, \boldsymbol{\epsilon}_i\}_{i=1}^N$, where $\boldsymbol{\mu}_i \equiv (\mu_{R,i}, \mu_{T,i})$ is the PMs of the i -th star, and $\boldsymbol{\epsilon}_i \equiv (\epsilon_{R,i}, \epsilon_{T,i})$ is the associated uncertainties, the posterior for the Gaussian parameters $\mathbf{p}_{\text{cl}} \equiv (\bar{\boldsymbol{\mu}}_{\text{cl}}, \boldsymbol{\sigma}_{\text{cl}}, \rho_{\text{cl}})$ and $\mathbf{p}_{\text{fg}} \equiv (\bar{\boldsymbol{\mu}}_{\text{fg}}, \boldsymbol{\sigma}_{\text{fg}}, \rho_{\text{fg}})$ is:

$$P(\mathbf{p}_{\text{cl}}, \mathbf{p}_{\text{fg}} | D) \propto P(D | \mathbf{p}_{\text{cl}}, \mathbf{p}_{\text{fg}}) P(\mathbf{p}_{\text{cl}}, \mathbf{p}_{\text{fg}}), \quad (17)$$

according to the Bayes' theorem, where $P(D | \mathbf{p}_{\text{cl}}, \mathbf{p}_{\text{fg}})$ is the likelihood and $P(\mathbf{p}_{\text{cl}}, \mathbf{p}_{\text{fg}})$ is the prior. The like-

lihood $P(D | \mathbf{p}_{\text{cl}}, \mathbf{p}_{\text{fg}})$ is a product of the two Gaussian mixtures for each data point:

$$P(D | \mathbf{p}_{\text{cl}}, \mathbf{p}_{\text{fg}}) \propto \prod_i \left[(1 - \eta) \mathcal{N}(\boldsymbol{\mu}_i; \bar{\boldsymbol{\mu}}_{\text{cl}}, \Sigma_{\text{cl},i}) + \eta \mathcal{N}(\boldsymbol{\mu}_i; \bar{\boldsymbol{\mu}}_{\text{fg}}, \Sigma_{\text{fg},i}) \right], \quad (18)$$

where η is the fraction of the foreground contaminants, $\mathcal{N}(\boldsymbol{\mu}_i; \bar{\boldsymbol{\mu}}, \Sigma_i)$ denotes the probability distribution function of a bivariate normal distribution characterized by a mean of $\bar{\boldsymbol{\mu}}$ and covariance of Σ_i evaluated for the i -th star with measured PMS $\boldsymbol{\mu}_i$. The covariance matrices of the i -th star $\Sigma_{\text{cl},i}$ and $\Sigma_{\text{fg},i}$ are associated with the measurement errors and intrinsic kinematics of the cluster and the foreground population, respectively:

$$\Sigma_{\text{cl},i} = \begin{bmatrix} \sigma_{R,\text{cl}}^2 + \epsilon_{R,i}^2 & \rho_{\text{cl}} \sigma_{R,\text{cl}} \sigma_{T,\text{cl}} \\ \rho_{\text{cl}} \sigma_{R,\text{cl}} \sigma_{T,\text{cl}} & \sigma_{T,\text{cl}}^2 + \epsilon_{T,i}^2 \end{bmatrix}, \quad (19)$$

$$\Sigma_{\text{fg},i} = \begin{bmatrix} \sigma_{R,\text{fg}}^2 + \epsilon_{R,i}^2 & \rho_{\text{fg}} \sigma_{R,\text{fg}} \sigma_{T,\text{fg}} \\ \rho_{\text{fg}} \sigma_{R,\text{fg}} \sigma_{T,\text{fg}} & \sigma_{T,\text{fg}}^2 + \epsilon_{T,i}^2 \end{bmatrix}. \quad (20)$$

In the case of the prior $P(\mathbf{p}_{\text{cl}}, \mathbf{p}_{\text{fg}})$, we adopt the non-informative Jeffreys priors for each bivariate Gaussian as follows (Berger & Sun 2008; Bernardo & Girón 1988):

$$P(\mathbf{p}_{\text{cl}}, \mathbf{p}_{\text{fg}}) \propto \frac{1}{\sqrt{(1 - \eta) \eta}} \prod_{k=\text{cl},\text{fg}} [\sigma_{R,k} \sigma_{T,k} (1 - \rho_k^2)]^{-2} \quad (21)$$

We determine the distribution of the posterior $P(\mathbf{p}_{\text{cl}}, \mathbf{p}_{\text{fg}} | D)$ utilizing the Markov chain Monte Carlo (MCMC) Ensemble sampler `emcee` (Foreman-Mackey et al. 2013).

We first draw a subsample of member candidates with high-quality PM measurements. The selection criteria are listed as follows:

- i. Synthetic PM measurement errors smaller than 0.2 mas yr^{-1} ;
- ii. Color membership cuts illustrated Figure 6;
- iii. Dereddened F160W_D brighter than 16 mag.

The kinematic membership probabilities are not involved in the sub-sampling process, which otherwise would bias the velocity dispersions in favor of smaller values. Instead, criteria ii and iii are adopted to minimize the fraction of foreground stars while ensuring completeness across the FOV. By these criteria, 1204 stars are selected, whose PMs are then transformed from x - y coordinates to radial (R) and tangential (T) components.

Table 5. Cluster Sample Size by Criteria

Catalog	Cut Type	Observed Stars	Weighted Stars ^a
Proper Motions	Detection in all Years	10,346	...
Proper Motion Box Cut	$v_x, v_y < 3\sigma_{pm}$	10002	...
Kinematic Probability Cut	$p_\mu \geq 0.3$	4341	...
Kinematic and Color Cut	$p_{clust} \geq 0.3$	3586	...
Radial Profile, Full Cluster	$1.00 M_\odot < M < 12.14 M_\odot, r_{eff} < 2.38 \text{ pc}$	1885	2404.9
Radial Profile, Low-Mass Bin	$1.00 M_\odot < M < 1.78 M_\odot$	738	1068.8
Radial Profile, Mid-Mass Bin	$1.78 M_\odot < M < 3.17 M_\odot$	634	801.2
Radial Profile, High-Mass Bin	$3.17 M_\odot < M < 12.14 M_\odot$	513	534.8
Radial Profile, Arches Comparison	$4.50 M_\odot < M < 12.14 M_\odot$	281	267.1
Radial Profile, Quintuplet Comparison	$2.50 M_\odot < M < 12.14 M_\odot$	757	830.7

^aThe weight refers to $w_i^{r_{eff}}$ in Equation 12 and requires the completeness and area fraction which is not yet calculated for the first four rows.**Table 6.** EFF Radial Profile Results

Sample	M	F160W _D	r_{eff} ^a	γ ^b	r_c ^c	a	Σ_0
	M_\odot	mag	pc		pc	pc	stars pc ⁻²
Full Cluster	1.00–12.14	17.50–11.52	≤ 2.38	$2.62^{+0.32}_{-0.26}$	0.78 ± 0.05	$0.93^{+0.13}_{-0.11}$	$588.78^{+35.41}_{-31.59}$
Low-Mass Bin	1.00–1.78	17.50–15.80	≤ 2.38	$2.69^{+0.78}_{-0.53}$	0.98 ± 0.09	$1.19^{+0.32}_{-0.25}$	$195.75^{+19.06}_{-15.06}$
Mid-Mass Bin	1.78–3.17	15.80–14.79	≤ 2.38	$2.97^{+0.77}_{-0.56}$	$0.77^{+0.08}_{-0.09}$	$1.00^{+0.27}_{-0.22}$	$207.14^{+24.57}_{-20.01}$
High-Mass Bin	3.17–12.14	14.79–11.52	≤ 2.38	$2.78^{+0.49}_{-0.38}$	$0.60^{+0.06}_{-0.07}$	$0.74^{+0.16}_{-0.13}$	$197.98^{+26.51}_{-20.47}$
Arches Comparison	4.5–12.14	14.03–17.50	≤ 2.38	$3.28^{+0.94}_{-0.66}$	$0.64^{+0.08}_{-0.09}$	$0.88^{+0.26}_{-0.21}$	$97.28^{+16.44}_{-13.03}$
Quint Comparison	2.5–12.14	15.29–17.50	≤ 2.38	$3.29^{+0.62}_{-0.47}$	0.70 ± 0.06	$0.96^{+0.18}_{-0.15}$	$258.73^{+24.45}_{-21.74}$

NOTE—Description of columns. *Sample*: Star sample used in corresponding analysis. *M*: Mass range of each sample. *F160W_D*: Dereddened magnitude in F160W. *r_{eff}*: Effective radius as defined in Equation 15. *γ*: Slope of the radial profile power law in Equation 13. *r_c*: Core radius in Equation 14. *a*: Core parameter converted from *r_c* and not sampled. *Σ₀*: Amplitude of the radial profile in Equation 13.^aRadius limit set by the distance at which the area fraction $f \geq 0.3$.^bUniform prior $U(1, 6)$.^cUniform prior $U(0, 2)$

We present the marginalized distributions of each parameter in Figure 17. Note that using uniform priors instead of the Jeffreys priors does not significantly impact our result. The fraction of foreground contaminants is estimated as low as $\sim 10 \pm 2\%$.

The mean PM in the radial and tangential component are $(\mu_{R,cl}, \mu_{T,cl}) = (0.03 \pm 0.01, -0.01 \pm 0.01) \text{ mas yr}^{-1}$, translating into $(0.48 \pm 0.19, -0.07 \pm 0.17) \text{ km s}^{-1}$ at a distance of 3077 pc, with positive tangential component corresponding to the counter-clockwise direction. The radial component is consistent with zero within 3- σ , indicating the positive value is statistically insignificant.

The radial PM is not found to increase with the radius from the cluster center either. Therefore, we find no evidence of expansion or contraction in the cluster, favoring the static scenario proposed by Gennaro et al. (2017).

The velocity dispersion measures to be $(\sigma_{R,cl}, \sigma_{T,cl}) = (0.24 \pm 0.01, 0.22 \pm 0.01) \text{ mas yr}^{-1}$, equivalent to $(3.57 \pm 0.15, 3.27 \pm 0.14) \text{ km s}^{-1}$ at the best-fit heliocentric distance 3077 pc. The 1D velocity dispersion is

$$\sigma_{1D} = \sqrt{\frac{\sigma_{R,cl}^2 + \sigma_{T,cl}^2}{2}} = 3.42 \pm 0.10 \text{ km s}^{-1}, \quad (22)$$

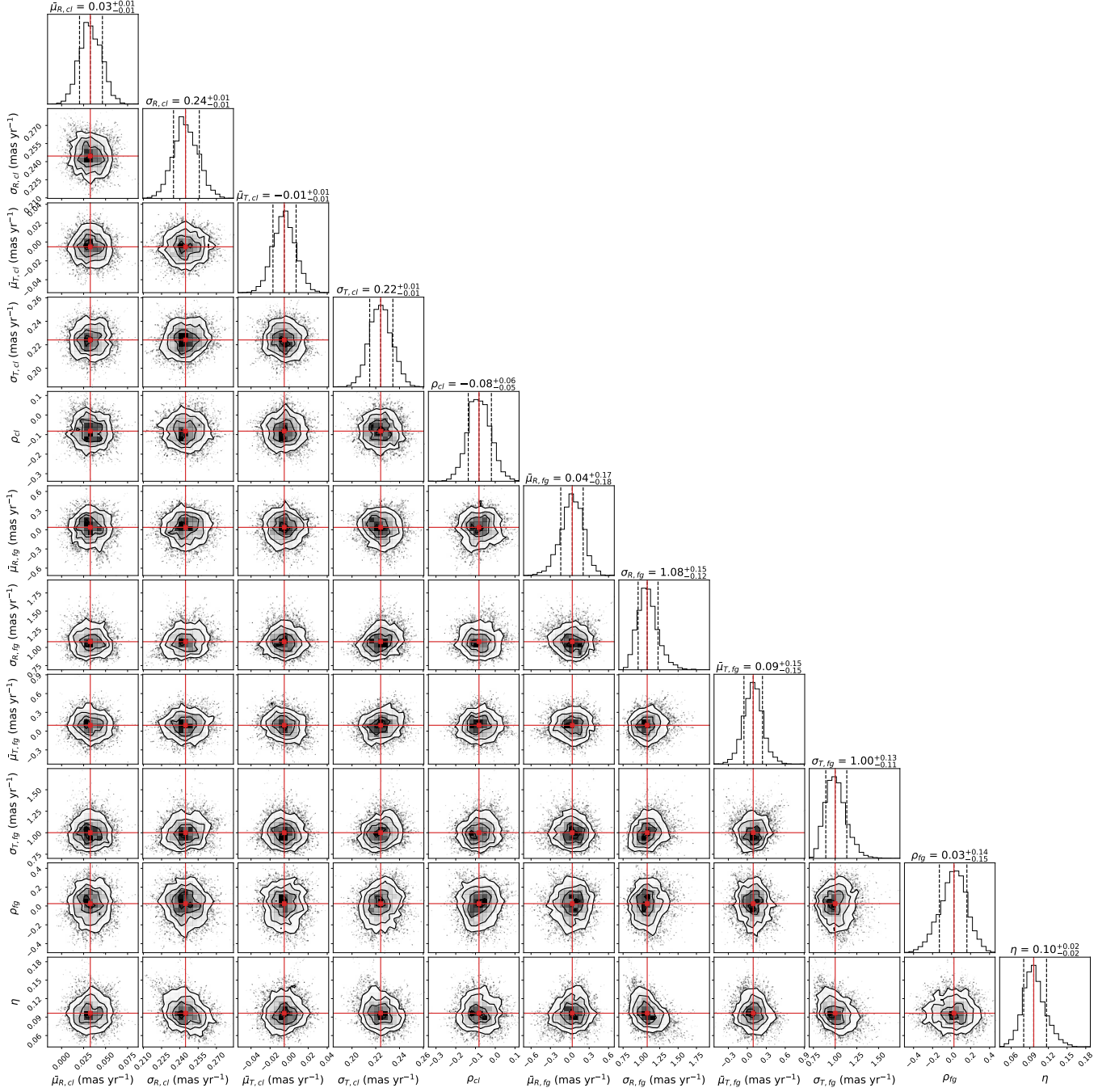


Figure 17. Marginalized posterior distributions for the parameters of kinematic modeling. The red line marks the median, and the dashed vertical lines mark the 16-th and 84-th percentiles.

or equivalently $0.23 \pm 0.01 \text{ mas yr}^{-1}$ at a distance of 3077 pc. We compare the velocity dispersion with virial equilibrium model in Section 6.2.

5.4. Mass Segregation

We investigate mass segregation in the cluster using two metrics: the mass segregation ratio and the core radii of the radial profiles from Section 5.2.

We model mass segregation in the cluster using the mass segregation ratio, Λ_{MSR} , developed by Allison et al. (2009), which is recognized as a reliable approach with the advantage of not requiring a center or overall stellar distribution (see Parker & Goodwin 2015, for further discussions). This method examines the degree of mass segregation by a ratio of the Minimum Spanning Tree (MST) length connecting the N_{MST} most massive

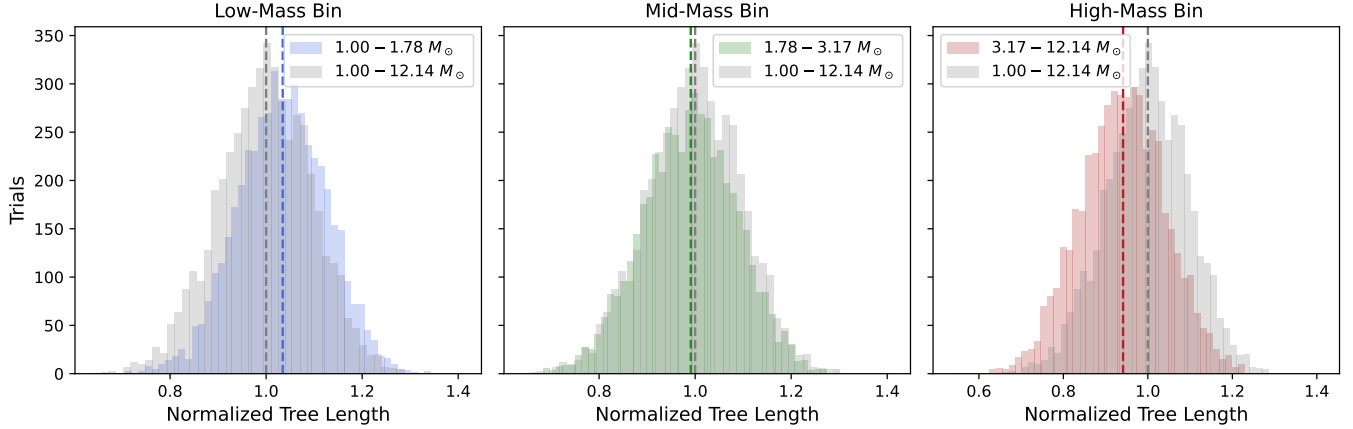


Figure 18. Distribution of MST lengths for our low-, mid-, and high-mass bins normalized by the mean MST length of the full catalog. *Left:* Low-mass bin. *Middle:* Mid-mass bin. *Right:* High-mass bin.

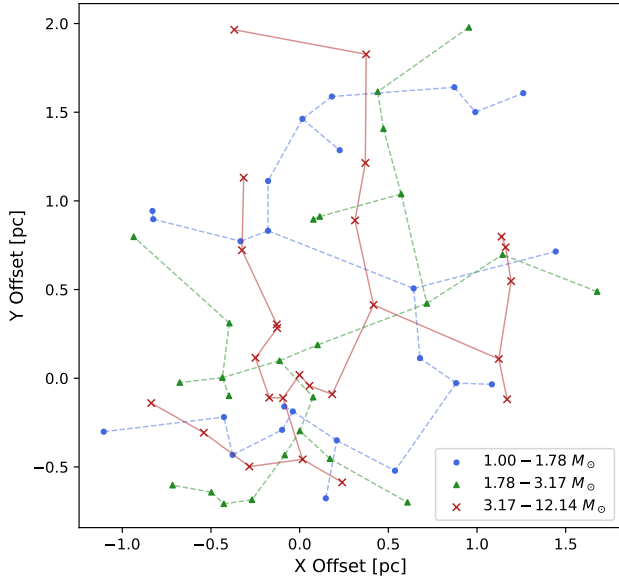


Figure 19. Minimum spanning tree in each mass bin with a tree length closest to the median normalized tree length in Figure 18. The high-mass stars are marked with *red x's*, the mid-mass stars are marked by *green triangles* and connected by *green dashed lines*, and the low-mass objects are marked with *blue circles* connected by *blue dotted lines*.

stars, l_{Massive} , to the mean MST length of N_{MST} random stars, $\langle l_{\text{norm}} \rangle$. The distribution of $\langle l_{\text{norm}} \rangle$ is roughly Gaussian and the error σ_{norm} is then taken to be the standard deviation of the distribution. The mass segregation ratio Λ_{MSR} is defined as:

$$\Lambda_{\text{MSR}} = \frac{\langle l_{\text{norm}} \rangle}{l_{\text{Massive}}} \pm \frac{\sigma_{\text{norm}}}{l_{\text{Massive}}} . \quad (23)$$

When Λ_{MSR} significantly differs significantly from 1, there is either mass segregation or inverse mass segre-

gation for values > 1 or < 1 , respectively. A value of 1 indicates no mass segregation in the cluster.

We modify this method by finding the distribution of l_{Massive} in a set of massive stars, rather than setting a fixed value of N_{MST} massive stars. We randomly sample this set of massive stars in the same way we sample the random set of stars and then compare the distributions of the MST length. In this way, we can characterize the distribution of minimum separations of the massive stars more comprehensively. Our updated mass segregation ratio is defined as:

$$\Lambda_{\text{MSR}} = \frac{\langle l_{\text{norm}} \rangle}{\langle l_{\text{Massive}} \rangle} \pm \sigma_{\text{MSR}} , \quad (24)$$

where

$$\sigma_{\text{MSR}} = \frac{\langle l_{\text{norm}} \rangle}{\langle l_{\text{Massive}} \rangle} \sqrt{\left(\frac{\sigma_{\text{norm}}}{\langle l_{\text{norm}} \rangle} \right)^2 + \left(\frac{\sigma_{\text{Massive}}}{\langle l_{\text{Massive}} \rangle} \right)^2} . \quad (25)$$

We utilize `scipy` to construct the MST. To ensure a smooth distribution of MST lengths, we perform 5000 trials of 25 randomly chosen stars for both sets of stars. All populations are comprised of cluster members with $p_{\text{clust}} \geq 0.3$. We account for the weight of each star by assigning the likelihood of selecting a given star proportional to its weight, as defined in equation 10.

Using the 200 brightest stars with $F160W_{\text{D}} \leq 13.6$ ($\approx 5.4 M_{\odot}$) in our sample as the set of massive stars, we find $\Lambda_{\text{MSR}} = 1.11 \pm 0.11$, slightly greater than 1 by only 1σ . We also notice that the mean MST lengths tend to decrease as the mean stellar mass increases, as shown in Figure 18, where we show the distributions of the MST length normalized by the mean of the full catalog for three mass bins. Figure 19 illustrates the MST of each mass bin closest to the median of their corresponding tree lengths.

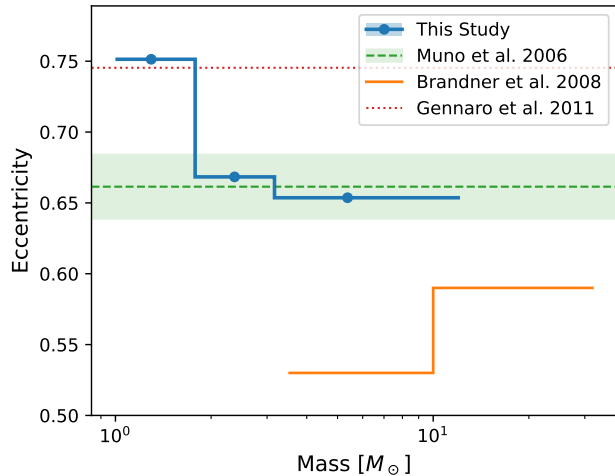


Figure 20. Eccentricity of the stellar density Gaussian profile as a function of stellar mass. The blue line shows the results of this study. The green dashed line and the shaded region mark the value and uncertainty derived in Muno et al. (2006). The amber line shows the measurements in Brandner et al. (2008). The overall eccentricity claimed by Gennaro et al. (2011) is marked as the red dotted line.

A similar trend is found in the posterior distributions of r_c in the EFF radial profile modeling, as shown in Figure 15. Two-sided Kolmogorov–Smirnov (KS) tests comparing the radii of the stars in each mass bin also indicate that they are drawn from different parent distributions. The p -values corresponding to the low-intermediate, low-high, and intermediate-high mass bin comparisons are 7.07×10^{-3} , 1.11×10^{-3} , and 6.33×10^{-11} , respectively, all of which are smaller than 3×10^{-2} . We therefore reject the null hypothesis that the radii are drawn from the same distribution and conclude that there is a low level of mass segregation present in the cluster within our mass range.

6. DISCUSSION

With the kinematic information derived in this work, we discuss the virial state, the relevant timescales of the cluster, and their implications.

6.1. Elongation

Our measured eccentricity of 0.71 is in good agreement with the value of 0.75 reported by Gennaro et al. (2011) and falls within the range of 0.68–0.72 identified by Andersen et al. (2017). Muno et al. (2006) reported a similar value of $e = 0.66 \pm 0.02$ by measuring the diffuse X-ray emissions of the cluster. In addition, we find the eccentricity decreases slightly with increasing mass, with $e = 0.75$, 0.67, and 0.65 for the low-, mid-, and high-mass bins, respectively, a trend that aligns with

the findings of Gennaro et al. (2011). Brandner et al. (2008) measured a moderately smaller e of 0.53 and 0.59 for the mass ranges of $3.5\text{--}10 M_\odot$ and $10\text{--}32 M_\odot$, respectively. The smaller eccentricity may stem from the bias introduced by the authors’ assumption about a point-symmetric half-mass radius. Instead, our measurement did not impose any assumption on the mass distribution. Different definitions of eccentricity and ellipticity are employed in the literature. In this work, we adopted the definition of ellipticity and eccentricity as described in Section 5.2. For consistency, we transformed the literature values to align with this definition for comparison. Figure 20 shows the comparison of values measured in this study and the literature.

The observed high eccentricity may result from the morphology of the molecular cloud within which Wd 1 forms, or imply a hierarchical formation pathway involving the merger of multiple substructures. The decreasing trend of eccentricity with increasing mass can be attributed to the shorter dynamical timescale of more massive stars as they are more concentrated in the center, which can be clearly observed in Figure 13. Therefore, more frequent interactions result in a more isotropic profile. Furthermore, as the elongation aligns with the galactic plane, this could also arise from the tidal stripping along the plane on less massive stars on the periphery of the cluster.

6.2. Virial State

Our measured velocity dispersion of $3.42 \pm 0.10 \text{ km s}^{-1}$ is smaller than the values expected for the cluster if it were in virial equilibrium $\sigma_{\text{vir}} = 4.5\text{--}6.5 \text{ km s}^{-1}$, suggesting that the cluster is subvirial. Brandner et al. (2008) estimated the virial equilibrium velocity dispersion to be $\sigma_{\text{vir}} \geq 4.5 \text{ km s}^{-1}$, or 0.25 mas yr^{-1} at their distance estimate of 3.55 kpc. Gennaro et al. (2011) and Gennaro et al. (2017) estimates $\sigma_{\text{vir}} = 4.5^{+0.8}_{-0.2} \text{ km s}^{-1}$, and Negueruela et al. (2010) reported 6.5 km s^{-1} (see Cottaar et al. 2012 for details). Note that the equilibrium velocity dispersion estimates depend on IMF extrapolations which need further confirmation. The virial velocity estimate would benefit from a more complete sample of low-mass objects in Wd 1. Assuming the current estimate of virial equilibrium velocity dispersion, Wd 1 would need to be at a distance of 4.0–5.8 kpc instead of 3077 pc for the observed velocity dispersion to match the virial equilibrium model. Though this work and recent estimates favor a closer distance (Aghakhanloo et al. 2021), the subvirial state of the Wd 1 cannot be definitively confirmed with the uncertainties in the IMF extrapolation and distance estimates.

In comparison, Mengel & Tacconi-Garman (2009) measured $\sigma_{1D} = 9.2 \pm 2.5 \text{ km s}^{-1}$ from 4 red supergiants, 5 yellow hypergiants, and a B-type emission line star. However, this result may be highly overestimated due to the presence of binaries (e.g., Kouwenhoven & de Grijs 2008; Gieles et al. 2010). Cottaar et al. (2012) reported $2.1_{-2.1}^{+3.3} \text{ km s}^{-1}$, which is derived from the spectroscopic measurements of several PMS stars. Our velocity dispersion measurement is derived from a significantly larger sample with membership and completeness correction. These improvements help mitigate potential biases and enhance the reliability and robustness of our results.

At the age of Wd 1, mass loss due to radiative feedback has already occurred and the cluster should be dynamically responding. The subvirial state of Wd 1, if present, with little gas remaining may imply that the star formation efficiency (SFE, the fraction of the initial gas mass that is turned into stars) is high enough at its formation for it to survive as a bound cluster. Previous studies find that eventually bound clusters are more likely to form in exceptionally high SFE environments, typically greater than 50% (Geyer & Burkert 2001; Li et al. 2019). However, there are arguments that up to half of the stars can remain bound with SFE smaller than 50% (Boily & Kroupa 2003).

Alternatively, cluster formation mechanisms can also explain the gravitationally bound state of Wd 1. Instead of forming in a static molecular cloud, stars can form in local overdensities such as gas filaments before they reach the forming star cluster (Bonnell et al. 2008; Longmore et al. 2014; Wei et al. 2024). Gas expulsion that already happens locally reduces the negative influence of stellar feedback on new star formation, resulting in bound clusters free of gas (Kruijssen 2012; Krause et al. 2020; Chevance et al. 2023). The high eccentricity of $e = 0.71$ of Wd 1 identified in this work may result from the merging of such local substructures during its formation.

6.3. Radial Profile Comparisons

We compare the radial profile of Wd 1 with the Arches and Quintuplet. We set a minimum mass limit of $4.5 M_{\odot}$ and $2.5 M_{\odot}$ to keep consistent mass ranges with Arches and Quintuplet, respectively. Details regarding the numbers of unweighted and weighted stars per bin and bin edges in mass are provided in Table 5.

Figure 21 shows the EFF radial profile comparisons with the Arches and Quintuplet, respectively. The masses are restricted to $> 4.5 M_{\odot}$ and $> 2.5 M_{\odot}$ for comparison consistency. The associated posteriors are illustrated in Figure 22.

6.4. Dynamical Timescales

In this section, we discuss the crossing time, relaxation time, the expected mass segregation timescales, and their implications on whether the mass segregation in Wd 1 is dynamical or primordial.

The crossing time of Wd 1 is

$$t_{\text{cross}} = \frac{R}{\sigma_{1D}} = 0.30 \text{ Myr} , \quad (26)$$

where we adopted the mean projected radius of $R = 1.0 \text{ pc}$, after excluding stars with an area fraction $f < 0.3$ used in modeling the velocity dispersion as in Section 5.3. This radius is consistent with the half-mass radius used in Brandner et al. (2008). In comparison, Gennaro et al. (2017) estimated a crossing time of 0.2 Myr assuming Wd 1 is virialized with a full radius of 2 pc. Our estimate results directly from the velocity dispersion measurements, without any assumption about the virial state. The age of Wd 1 is therefore about 36 times its crossing time.

The relaxation time can be calculated from the number of stars N and the crossing time t_{cross} (Binney & Tremaine 2008),

$$t_{\text{relax}} = \frac{N}{10 \ln N} t_{\text{cross}} = 0.26 \text{ Gyr} , \quad (27)$$

where we assume the total number of stars is $N \sim 10^5$ (Brandner et al. 2008; Gennaro et al. 2017). This is about 24 times the age of Wd 1.

The timescale for a star of mass M to reach energy equipartition and therefore dynamical mass segregation is

$$t(M) \sim \frac{\bar{m}}{M} t_{\text{relax}} , \quad (28)$$

where \bar{m} is the average mass of the cluster. Considering the cluster age of 10.7 Myr and an average mass of $\sim 0.4 M_{\odot}$ (Gennaro et al. 2017), we would expect mass segregation for stars more massive than $\sim 10 M_{\odot}$. In comparison, Cottaar et al. (2012) estimated a segregation mass of $20 M_{\odot}$, and Gennaro et al. (2017) reported little or no mass segregation except for the $> 40 M_{\odot}$ stars in Wd 1 based on observation. Recall that our analysis is restricted to stars in the mass range of $1.00\text{--}12.14 M_{\odot}$, which may account for the lack of significant segregation observed in this study. With a mass segregation ratio of $\Lambda_{\text{MSR}} = 1.11 \pm 0.11$, only marginally greater than 1 by $1\text{--}\sigma$. This is consistent with the expectation from the timescale analysis that the stellar population in this mass range does not exhibit strong segregation.

The consistency between the observed minor mass segregation in the lower mass range, combined with the segregation mass estimates based on dynamical timescales,

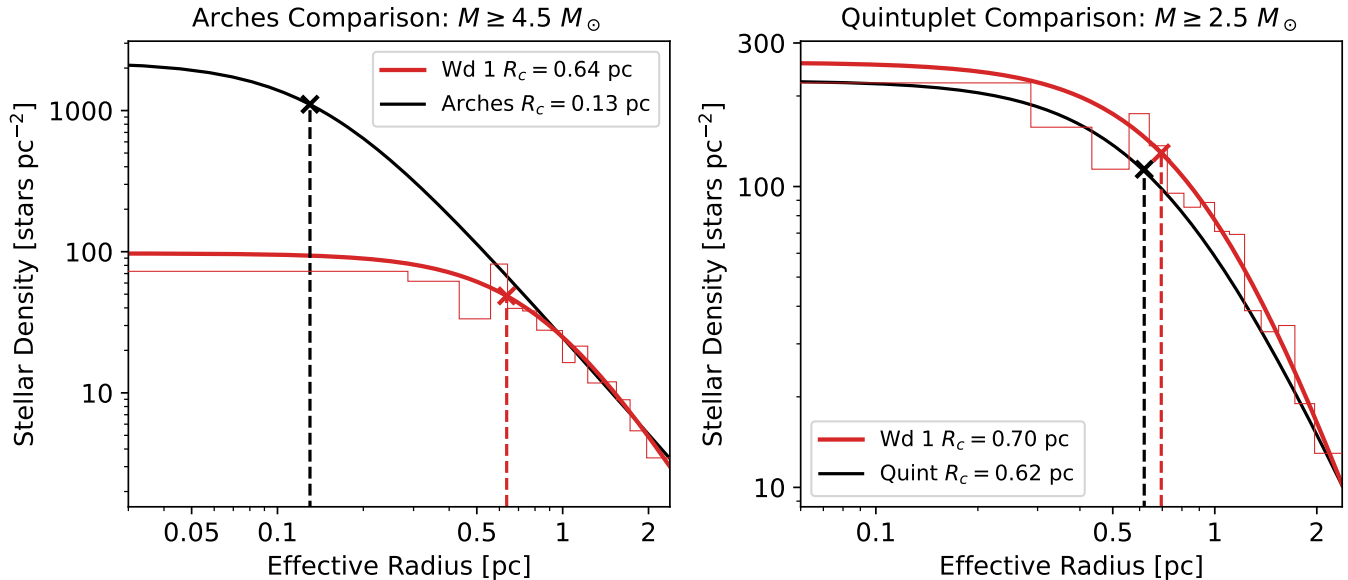


Figure 21. Comparison of the radial profile of Wd 1 to the Arches and Quintuplet clusters using the EFF fit parameters in Hosek et al. (2015) and Rui et al. (2019). We restrict the profile fit to $M > 4.5 M_{\odot}$ and $M > 2.5 M_{\odot}$ for the Arches and Quintuplet comparison, respectively.

implies that the segregation in Wd 1 is likely dynamical rather than primordial, in agreement with previous studies (Gennaro et al. 2017). The dynamical process in this mass range is possibly still ongoing considering its age and relaxation timescale. The highest-mass stars are already segregated, and lower-mass stars are beginning to experience the effects of dynamical processes, therefore displaying a weak sign of mass segregation.

7. CONCLUSION

We analyze the kinematics and structure of Wd 1 using the multi-epoch astrometric and photometric data from HST WFC3-IR filters. We model the kinematic and color membership of the stars. The structure of Wd 1 is thoroughly analyzed after correcting for membership, extinction, and completeness. Specifically, we report the following conclusions.

- i. We obtained the cluster membership of 10,346 observed stars, consisting of PM kinematic membership characterized by a 3-component GMM model, a boolean photometric membership, and completeness correction.
- ii. We construct the stellar density map of Wd 1 corrected by a spatial reddening map and cluster membership of each star.
- iii. With the stellar density map, we find that the cluster is elongated in a northeast-southwest direction, aligning with the galactic plane, with an eccentricity of 0.71 and the semi-major axis at a

position angle of $\sim 56^{\circ}$ east of north, which aligns with the galactic plane. Furthermore, eccentricity decreases with increasing mass.

- iv. The high eccentricity may be inherited from the molecular cloud from which Wd 1 formed, or imply a formation process during which multiple substructures merged. The alignment of the elongation with the galactic plane, coupled with the higher eccentricity and more spatially diffuse distribution of low-mass stars, may also indicate tidal disruption within the galactic plane.
- v. We fit an EFF radial profile model to the stellar density and observed a slight decrease in the core radius with increasing stellar mass, indicative of a minor mass segregation.
- vi. Another weak sign of mass segregation is identified by comparing the MST length for different mass ranges, with a relatively small mass segregation ratio of $\Lambda_{\text{MSR}} = 1.11 \pm 0.11$.
- vii. We present the velocity dispersion measurements for 1,204 stars. The velocity dispersion is $(\sigma_{R,cl}, \sigma_{T,cl}) = (0.24 \pm 0.01, 0.22 \pm 0.01) \text{ mas yr}^{-1}$, translating into $(3.57 \pm 0.15, 3.27 \pm 0.14) \text{ km s}^{-1}$. The 1D velocity dispersion of $\sigma_{1D} = 3.42 \pm 0.10 \text{ km s}^{-1}$ is below the virial equilibrium estimate of $\sigma_{\text{vir}} = 4.5\text{--}6.5 \text{ km s}^{-1}$ reported in the literature, suggesting the cluster is subvirial.

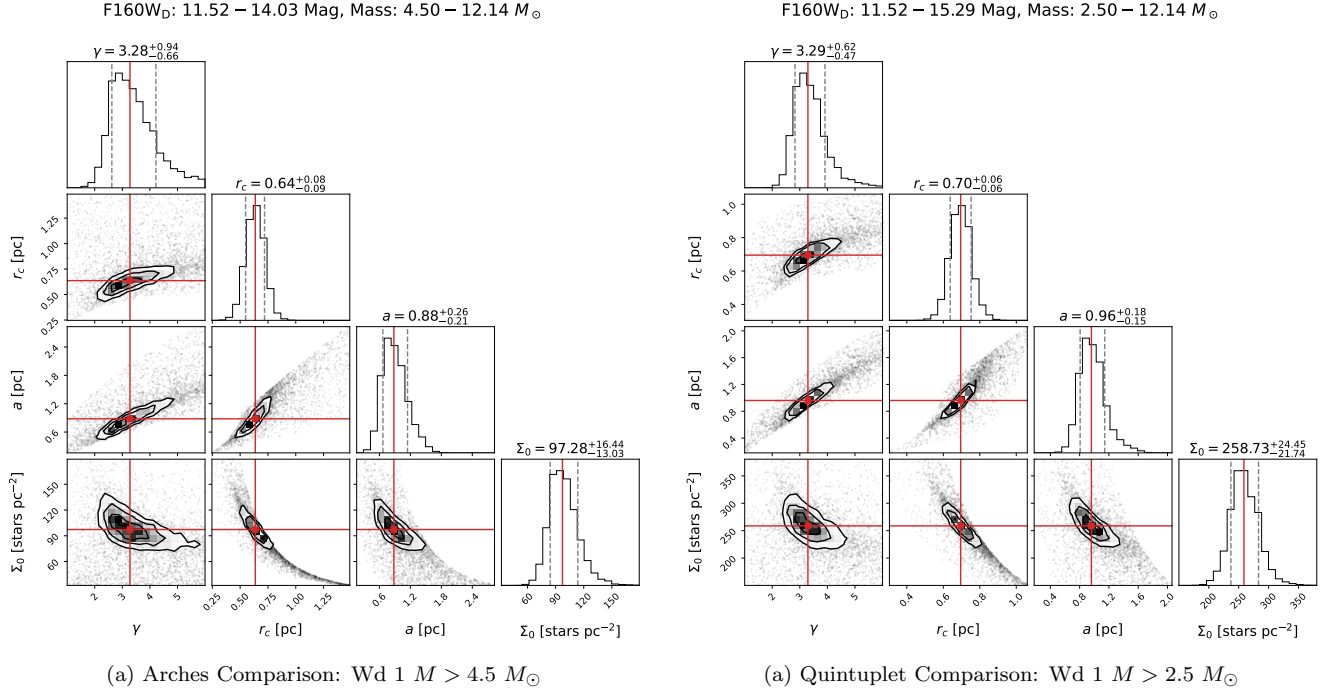


Figure 22. Weighted posterior distributions of EFF radial profile parameters. (a): Sources with mass greater than $4.5 M_{\odot}$ for comparison with the Arches cluster. (b): Sources with mass greater than $2.5 M_{\odot}$ for comparison with the Quintuplet cluster. The red lines mark the weighted median, and the gray dashed line marks the weighted 16- and 84-th percentiles. Note that we only modeled r_c , and the posterior distribution of a is purely converted from r_c .

- viii. The subvirial, gravitationally bound state of Wd 1 with little gas remaining implies either an exceptionally high SFE likely $> 50\%$ at its formation, or it forms from the merging of substructures like gas filaments that already started local gas expulsion driven by stellar feedback before they reach the cluster.
- ix. The crossing time is 0.30 Myr with a mean projected cluster radius of $R = 1.0$ pc weighted by membership, completeness, and area fraction. The age of Wd 1 at 10.7 Myr is about 36 times its crossing time. The relaxation time is 0.26 Gyr, about 24 times its age.
- x. Given the age and relaxation time, we expect mass segregation for stars down to $10 M_{\odot}$, which accounts for the weak sign of segregation in our analysis with $\Lambda_{\text{MSR}} = 1.11 \pm 0.11$, as this work is restricted to sources between the mass range of 1.00–12.14 M_{\odot} . This implies that mass segregation is more likely dynamical rather than primordial in Wd 1.

Facility: HST WFC3

Software: `astropy` (Astropy Collaboration et al. 2018, 2022), `PyMultiNest` (Buchner 2016), `emcee` (Foreman-Mackey et al. 2013), `Matplotlib` (Hunter 2007)

This research is based on observations made with the NASA/ESA Hubble Space Telescope obtained from the Space Telescope Science Institute (STScI), which is operated by the Association of Universities for Research in Astronomy, Inc., under NASA contract NAS 526555. We acknowledge support for this work from NASA and STScI through program numbers GO-13044 and GO-13809. J.R.L., P.C.B., D.K., and M.S. acknowledge support from the National Science Foundation Astronomy and Astrophysics Grant AST-1764218. N.Z.R. acknowledges support from the National Science Foundation Graduate Research Fellowship under Grant No. DGE-1745301. Portions of this work were conducted at the University of California, San Diego, which was built on the unceded territory of the Kumeyaay Nation, whose people continue to maintain their political sovereignty and cultural traditions as vital members of the San Diego community.

REFERENCES

- Aghakhanloo, M., Murphy, J. W., Smith, N., et al. 2020, *MNRAS*, 492, 2497, doi: [10.1093/mnras/stz3628](https://doi.org/10.1093/mnras/stz3628)
- . 2021, *Research Notes of the American Astronomical Society*, 5, 14, doi: [10.3847/2515-5172/abdc2c](https://doi.org/10.3847/2515-5172/abdc2c)
- Allison, R. J., Goodwin, S. P., Parker, R. J., et al. 2009, *MNRAS*, 395, 1449, doi: [10.1111/j.1365-2966.2009.14508.x](https://doi.org/10.1111/j.1365-2966.2009.14508.x)
- Andersen, M. 2009, Determining the Sub-stellar IMF in the Most Massive Young Milky Way Cluster, Westerlund 1, HST Proposal ID 11708. Cycle 17
- Andersen, M., Gennaro, M., Brandner, W., et al. 2017, *A&A*, 602, A22, doi: [10.1051/0004-6361/201322863](https://doi.org/10.1051/0004-6361/201322863)
- Anderson, J. 2022, One-Pass HST Photometry with hst1pass, Instrument Science Report WFC3 2022-5, 55 pages
- Anderson, J., & King, I. R. 2006, PSFs, Photometry, and Astronomy for the ACS/WFC, Instrument Science Report ACS 2006-01, 34 pages
- Anderson, J., Sarajedini, A., Bedin, L. R., et al. 2008, *AJ*, 135, 2055, doi: [10.1088/0004-6256/135/6/2055](https://doi.org/10.1088/0004-6256/135/6/2055)
- Astropy Collaboration, Price-Whelan, A. M., Sipőcz, B. M., et al. 2018, *AJ*, 156, 123, doi: [10.3847/1538-3881/aabc4f](https://doi.org/10.3847/1538-3881/aabc4f)
- Astropy Collaboration, Price-Whelan, A. M., Lim, P. L., et al. 2022, *ApJ*, 935, 167, doi: [10.3847/1538-4357/ac7c74](https://doi.org/10.3847/1538-4357/ac7c74)
- Beasor, E. R., Davies, B., Smith, N., & Bastian, N. 2019, *MNRAS*, 486, 266, doi: [10.1093/mnras/stz732](https://doi.org/10.1093/mnras/stz732)
- Beasor, E. R., Davies, B., Smith, N., Gehrz, R. D., & Figer, D. F. 2021, *ApJ*, 912, 16, doi: [10.3847/1538-4357/abec44](https://doi.org/10.3847/1538-4357/abec44)
- Bellini, A., Anderson, J., Bedin, L. R., et al. 2017, *ApJ*, 842, 6, doi: [10.3847/1538-4357/aa7059](https://doi.org/10.3847/1538-4357/aa7059)
- Bellini, A., Libralato, M., Bedin, L. R., et al. 2018, *ApJ*, 853, 86, doi: [10.3847/1538-4357/aaa3ec](https://doi.org/10.3847/1538-4357/aaa3ec)
- Berger, J. O., & Sun, D. 2008, arXiv e-prints, arXiv:0804.0987, doi: [10.48550/arXiv.0804.0987](https://doi.org/10.48550/arXiv.0804.0987)
- Bernardo, J. M., & Girón, F. J. 1988, *Bayesian Statistics 3*, 67
- Binney, J., & Tremaine, S. 2008, *Galactic Dynamics: Second Edition*
- Boily, C. M., & Kroupa, P. 2003, *MNRAS*, 338, 665, doi: [10.1046/j.1365-8711.2003.06076.x](https://doi.org/10.1046/j.1365-8711.2003.06076.x)
- Bonnell, I. A., Clark, P., & Bate, M. R. 2008, *MNRAS*, 389, 1556, doi: [10.1111/j.1365-2966.2008.13679.x](https://doi.org/10.1111/j.1365-2966.2008.13679.x)
- Brandner, W., Clark, J. S., Stolte, A., et al. 2008, *A&A*, 478, 137, doi: [10.1051/0004-6361:20077579](https://doi.org/10.1051/0004-6361:20077579)
- Bressan, A., Marigo, P., Girardi, L., et al. 2012, *MNRAS*, 427, 127, doi: [10.1111/j.1365-2966.2012.21948.x](https://doi.org/10.1111/j.1365-2966.2012.21948.x)
- Buchner, J. 2016, PyMultiNest: Python interface for MultiNest, Astrophysics Source Code Library, record ascl:1606.005
- Buchner, J., Georgakakis, A., Nandra, K., et al. 2014, *A&A*, 564, A125, doi: [10.1051/0004-6361/201322971](https://doi.org/10.1051/0004-6361/201322971)
- Chevance, M., Krumholz, M. R., McLeod, A. F., et al. 2023, in *Astronomical Society of the Pacific Conference Series*, Vol. 534, Protostars and Planets VII, ed. S. Inutsuka, Y. Aikawa, T. Muto, K. Tomida, & M. Tamura, 1
- Cicuéndez, L., Battaglia, G., Irwin, M., et al. 2018, *A&A*, 609, A53, doi: [10.1051/0004-6361/201731450](https://doi.org/10.1051/0004-6361/201731450)
- Clark, J. S., Negueruela, I., Crowther, P. A., & Goodwin, S. P. 2005, *A&A*, 434, 949, doi: [10.1051/0004-6361:20042413](https://doi.org/10.1051/0004-6361:20042413)
- Clarkson, W. I., Ghez, A. M., Morris, M. R., et al. 2012, *ApJ*, 751, 132, doi: [10.1088/0004-637X/751/2/132](https://doi.org/10.1088/0004-637X/751/2/132)
- Cottaar, M., Meyer, M. R., Andersen, M., & Espinoza, P. 2012, *A&A*, 539, A5, doi: [10.1051/0004-6361/201117722](https://doi.org/10.1051/0004-6361/201117722)
- Crowther, P. A., Hadfield, L. J., Clark, J. S., Negueruela, I., & Vacca, W. D. 2006, *MNRAS*, 372, 1407, doi: [10.1111/j.1365-2966.2006.10952.x](https://doi.org/10.1111/j.1365-2966.2006.10952.x)
- Davies, B., & Beasor, E. R. 2019, *MNRAS*, 486, L10, doi: [10.1093/mnrasl/slz050](https://doi.org/10.1093/mnrasl/slz050)
- de Grijs, R. 2004, Our Galaxy's most promising Super Star Cluster candidate, Westerlund 1: Tip of the Iceberg?, HST Proposal ID 10172. Cycle 13
- Do, T., Lu, J. R., Ghez, A. M., et al. 2013, *ApJ*, 764, 154, doi: [10.1088/0004-637X/764/2/154](https://doi.org/10.1088/0004-637X/764/2/154)
- Eldridge, J. J., Stanway, E. R., Xiao, L., et al. 2017, *PASA*, 34, e058, doi: [10.1017/pasa.2017.51](https://doi.org/10.1017/pasa.2017.51)
- Elson, R. A. W., Fall, S. M., & Freeman, K. C. 1987, *ApJ*, 323, 54, doi: [10.1086/165807](https://doi.org/10.1086/165807)
- Feroz, F., Hobson, M. P., & Bridges, M. 2009, *MNRAS*, 398, 1601, doi: [10.1111/j.1365-2966.2009.14548.x](https://doi.org/10.1111/j.1365-2966.2009.14548.x)
- Foreman-Mackey, D., Hogg, D. W., Lang, D., & Goodman, J. 2013, *PASP*, 125, 306, doi: [10.1086/670067](https://doi.org/10.1086/670067)
- Gennaro, M., Brandner, W., Stolte, A., & Henning, T. 2011, *MNRAS*, 412, 2469, doi: [10.1111/j.1365-2966.2010.18068.x](https://doi.org/10.1111/j.1365-2966.2010.18068.x)
- Gennaro, M., Goodwin, S. P., Parker, R. J., Allison, R. J., & Brandner, W. 2017, *MNRAS*, 472, 1760, doi: [10.1093/mnras/stx2098](https://doi.org/10.1093/mnras/stx2098)
- Geyer, M. P., & Burkert, A. 2001, *MNRAS*, 323, 988, doi: [10.1046/j.1365-8711.2001.04257.x](https://doi.org/10.1046/j.1365-8711.2001.04257.x)
- Ghez, A. M., Salim, S., Hornstein, S. D., et al. 2005, *ApJ*, 620, 744, doi: [10.1086/427175](https://doi.org/10.1086/427175)
- Gieles, M., Sana, H., & Portegies Zwart, S. F. 2010, *MNRAS*, 402, 1750, doi: [10.1111/j.1365-2966.2009.15993.x](https://doi.org/10.1111/j.1365-2966.2009.15993.x)
- Hosek, Jr., M. W., Lu, J. R., Anderson, J., et al. 2015, *ApJ*, 813, 27, doi: [10.1088/0004-637X/813/1/27](https://doi.org/10.1088/0004-637X/813/1/27)
- . 2019, *ApJ*, 870, 44, doi: [10.3847/1538-4357/aaef90](https://doi.org/10.3847/1538-4357/aaef90)

- Hunter, J. D. 2007, *Computing in Science and Engineering*, 9, 90, doi: [10.1109/MCSE.2007.55](https://doi.org/10.1109/MCSE.2007.55)
- Kothes, R., & Dougherty, S. M. 2007, *A&A*, 468, 993, doi: [10.1051/0004-6361:20077309](https://doi.org/10.1051/0004-6361:20077309)
- Koumpia, E., & Bonanos, A. Z. 2012, *A&A*, 547, A30, doi: [10.1051/0004-6361/201219465](https://doi.org/10.1051/0004-6361/201219465)
- Kouwenhoven, M. B. N., & de Grijs, R. 2008, *A&A*, 480, 103, doi: [10.1051/0004-6361:20078897](https://doi.org/10.1051/0004-6361:20078897)
- Krause, M. G. H., Offner, S. S. R., Charbonnel, C., et al. 2020, *SSRv*, 216, 64, doi: [10.1007/s11214-020-00689-4](https://doi.org/10.1007/s11214-020-00689-4)
- Kruijssen, J. M. D. 2012, *MNRAS*, 426, 3008, doi: [10.1111/j.1365-2966.2012.21923.x](https://doi.org/10.1111/j.1365-2966.2012.21923.x)
- Li, H., Vogelsberger, M., Marinacci, F., & Gnedin, O. Y. 2019, *MNRAS*, 487, 364, doi: [10.1093/mnras/stz1271](https://doi.org/10.1093/mnras/stz1271)
- Lim, B., Chun, M.-Y., Sung, H., et al. 2013, *AJ*, 145, 46, doi: [10.1088/0004-6256/145/2/46](https://doi.org/10.1088/0004-6256/145/2/46)
- Longmore, S. N., Kruijssen, J. M. D., Bastian, N., et al. 2014, in *Protostars and Planets VI*, ed. H. Beuther, R. S. Klessen, C. P. Dullemond, & T. Henning, 291–314
- Lu, J. R., Anderson, J., Clarkson, W. I., et al. 2016a, *The IMF and Internal Kinematics of the Massive Young Star Cluster, Westerlund 1, HST Proposal. Cycle 20, ID. #13044*
- . 2016b, *The IMF and Internal Kinematics of the Massive Young Star Cluster, Westerlund 1, HST Proposal. Cycle 22, ID. #13809*
- Lu, J. R., Do, T., Ghez, A. M., et al. 2013, *ApJ*, 764, 155, doi: [10.1088/0004-637X/764/2/155](https://doi.org/10.1088/0004-637X/764/2/155)
- Lu, J. R., Ghez, A. M., Hornstein, S. D., et al. 2009, *ApJ*, 690, 1463, doi: [10.1088/0004-637X/690/2/1463](https://doi.org/10.1088/0004-637X/690/2/1463)
- Mackey, A. D., & Gilmore, G. F. 2003a, *MNRAS*, 338, 85, doi: [10.1046/j.1365-8711.2003.06021.x](https://doi.org/10.1046/j.1365-8711.2003.06021.x)
- . 2003b, *MNRAS*, 338, 120, doi: [10.1046/j.1365-8711.2003.06022.x](https://doi.org/10.1046/j.1365-8711.2003.06022.x)
- McLaughlin, D. E., & van der Marel, R. P. 2005, *ApJS*, 161, 304, doi: [10.1086/497429](https://doi.org/10.1086/497429)
- Mengel, S., & Tacconi-Garman, L. E. 2009, *Ap&SS*, 324, 321, doi: [10.1007/s10509-009-0106-7](https://doi.org/10.1007/s10509-009-0106-7)
- Muno, M. P., Law, C., Clark, J. S., et al. 2006, *The Astrophysical Journal*, 650, 203, doi: [10.1086/507175](https://doi.org/10.1086/507175)
- Navarete, F., Daminieli, A., Ramirez, A. E., Rocha, D. F., & Almeida, L. A. 2022, *MNRAS*, 516, 1289, doi: [10.1093/mnras/stac2374](https://doi.org/10.1093/mnras/stac2374)
- Negueruela, I., Clark, J. S., & Ritchie, B. W. 2010, *A&A*, 516, A78, doi: [10.1051/0004-6361/201014032](https://doi.org/10.1051/0004-6361/201014032)
- Parker, R. J., & Goodwin, S. P. 2015, *MNRAS*, 449, 3381, doi: [10.1093/mnras/stv539](https://doi.org/10.1093/mnras/stv539)
- Portegies Zwart, S. F., McMillan, S. L. W., & Gieles, M. 2010, *ARA&A*, 48, 431, doi: [10.1146/annurev-astro-081309-130834](https://doi.org/10.1146/annurev-astro-081309-130834)
- Richardson, J. C., Irwin, M. J., McConnachie, A. W., et al. 2011, *ApJ*, 732, 76, doi: [10.1088/0004-637X/732/2/76](https://doi.org/10.1088/0004-637X/732/2/76)
- Rocha, D. F., Almeida, L. A., Daminieli, A., et al. 2022, *MNRAS*, 517, 3749, doi: [10.1093/mnras/stac2927](https://doi.org/10.1093/mnras/stac2927)
- Rui, N. Z., Hosek, Matthew W., J., Lu, J. R., et al. 2019, *ApJ*, 877, 37, doi: [10.3847/1538-4357/ab17e0](https://doi.org/10.3847/1538-4357/ab17e0)
- Schwarz, G. 1978, *Ann. Statist.*, 6, 461, doi: [10.1214/aos/1176344136](https://doi.org/10.1214/aos/1176344136)
- Wei, L., Theissen, C. A., Konopacky, Q. M., et al. 2024, *ApJ*, 962, 174, doi: [10.3847/1538-4357/ad1401](https://doi.org/10.3847/1538-4357/ad1401)
- Westerlund, B. 1961, *PASP*, 73, 51, doi: [10.1086/127618](https://doi.org/10.1086/127618)
- Yelda, S., Ghez, A. M., Lu, J. R., et al. 2014, *ApJ*, 783, 131, doi: [10.1088/0004-637X/783/2/131](https://doi.org/10.1088/0004-637X/783/2/131)